

Electrically driven spin resonance of 4f electrons in a single atom on a surface

Received: 9 October 2023

Accepted: 5 June 2024

Published online: 20 June 2024

 Check for updatesStefano Reale ^{1,2,3}, Jiyeon Hwang^{1,4}, Jeongmin Oh ^{1,4}, Harald Brune ⁵,
Andreas J. Heinrich ^{1,4}, Fabio Donati ^{1,4} ✉ & Yujeong Bae ^{1,4,6} ✉

A pivotal challenge in quantum technologies lies in reconciling long coherence times with efficient manipulation of the quantum states of a system. Lanthanide atoms, with their well-localized 4f electrons, emerge as a promising solution to this dilemma if provided with a rational design for manipulation and detection. Here we construct tailored spin structures to perform electron spin resonance on a single lanthanide atom using a scanning tunneling microscope. A magnetically coupled structure made of an erbium and a titanium atom enables us to both drive the erbium's 4f electron spins and indirectly probe them through the titanium's 3d electrons. The erbium spin states exhibit an extended spin relaxation time and a higher driving efficiency compared to 3d atoms with spin 1/2 in similarly coupled structures. Our work provides a new approach to accessing highly protected spin states, enabling their coherent control in an all-electric fashion.

The last two decades have witnessed a rising focus on the control and application of quantum coherent effects, marking the advent of the so-called “second quantum revolution”. Utilizing quantum coherent functionalities of materials for novel technologies, such as imaging, information processing, and communications, requires robustness of their quantum coherence, addressability, and scalability¹. However, these requirements often clash since decoupling the quantum states from the environment prolongs the quantum coherent properties but hinders the possibility of efficient state manipulation.

Lanthanide atoms represent a promising platform to tackle this dilemma. Their well-localized 4f electrons show long spin relaxation T_1 ^{2,3} and coherence times T_2 ^{4,5}. In addition, their strong hyperfine interaction facilitates the read-out of nuclear spins^{6,7}. In bulk insulators, exceedingly long T_1 and T_2 have been demonstrated using optical control and detection^{8–11} down to the single atom level^{12,13}. While hybrid optical-electrical approaches have been developed to access individual lanthanide atom's spins embedded in a silicon transistor¹⁴, it is still challenging to achieve efficient control of the quantum states using electrical transport methods. This necessitates the rational design of a quantum platform capable of tackling both control and detection

schemes, along with their interactions with local environments. In this context, single crystal surfaces constitute an advantageous framework both for building atomically engineered nanostructures and addressing individual spin centers, in particular using scanning probe techniques^{15–18}. However, resonant driving and detection of surface-adsorbed lanthanide atoms have so far remained elusive.

In this work, we demonstrate the control and detection of 4f electron spins by building atomic-scale structures on a surface using a scanning tunneling microscope (STM) with electron spin resonance (ESR) capabilities^{19–22}. The atomic structures are composed of an erbium (Er) atom as the target spin system and a magnetically coupled titanium (Ti) atom as the sensor spin. This architecture allows us to drive ESR transitions on the Er 4f electrons with a projected angular momentum of $\hbar/2$ ²³ and to probe them indirectly through Ti. We observed an Er T_1 of close to 1 μ s, which is about 5 times longer than that previously measured for 3d electrons of a remotely-driven spin-1/2 system on the same surface¹⁸. This novel platform allows for the ESR driving and read-out of the well-screened 4f electron spin states, paving the way to integrate lanthanide atoms in quantum architectures.

¹Center for Quantum Nanoscience (QNS), Institute for Basic Science (IBS), Seoul, Republic of Korea. ²Ewha Womans University, Seoul, Republic of Korea.

³Department of Energy, Politecnico di Milano, Milano, Italy. ⁴Department of Physics, Ewha Womans University, Seoul, Republic of Korea. ⁵Institute of Physics, Ecole Polytechnique Fédérale de Lausanne, Lausanne, Switzerland. ⁶Present address: Empa, Swiss Federal Laboratories for Materials Science and Technology, nanotech@surfaces Laboratory, Dübendorf, Switzerland. ✉ e-mail: donati.fabio@qns.science; bae.yujeong@qns.science

Results

Sensing Er Spin States through a Ti Atom

Erbium atoms on a few monolayer-thick MgO(100) on Ag(100) present a $4f^{11}$ configuration with no unpaired electrons in the $5d$ and $6s$ shells²³. The atomic-like spin and orbital momenta are coupled through the large spin-orbit interaction into a total angular momentum \mathbf{J}_{Er} with magnitude of $15\hbar/2$ ²³. When adsorbed on the oxygen site of MgO (Fig. 1a), the crystal field leads to a strong hard-axis magneto-crystalline anisotropy that stabilizes a doubly-degenerate ground state with an out-of-plane component of the angular momentum $J_{\perp} = \pm\hbar/2$ ²³, which splits into two singlets when an external magnetic field (\mathbf{B}) is applied. This magnetic level scheme differs from the ones of lanthanide single atom

magnets studied so far on MgO/Ag(100). For instance, dysprosium^{24,25} and holmium^{2,26,27} present a ground state characterized by a large J_{\perp} . The level scheme presents two lowest-lying states well separated by a significant anisotropy barrier and greatly suppresses the reversal of angular momentum, thereby stabilizing the magnetic states. Additionally, it impedes the first-order ESR transition induced by the exchange of a single quantum of angular momentum²². As found in a previous work²³, the component of \mathbf{J}_{Er} along the magnetic field direction (z), defined as J_z , increases from $\pm\hbar/2$ to $\pm 4\hbar$ by rotating \mathbf{B} from the out-of-plane ($\vartheta = 0^\circ$) to the in-plane ($\vartheta = 90^\circ$) direction (Fig. 1b), while retaining a large probability for spin dipole transitions. Given these properties, Er can be regarded as a highly tunable two-level system allowing for

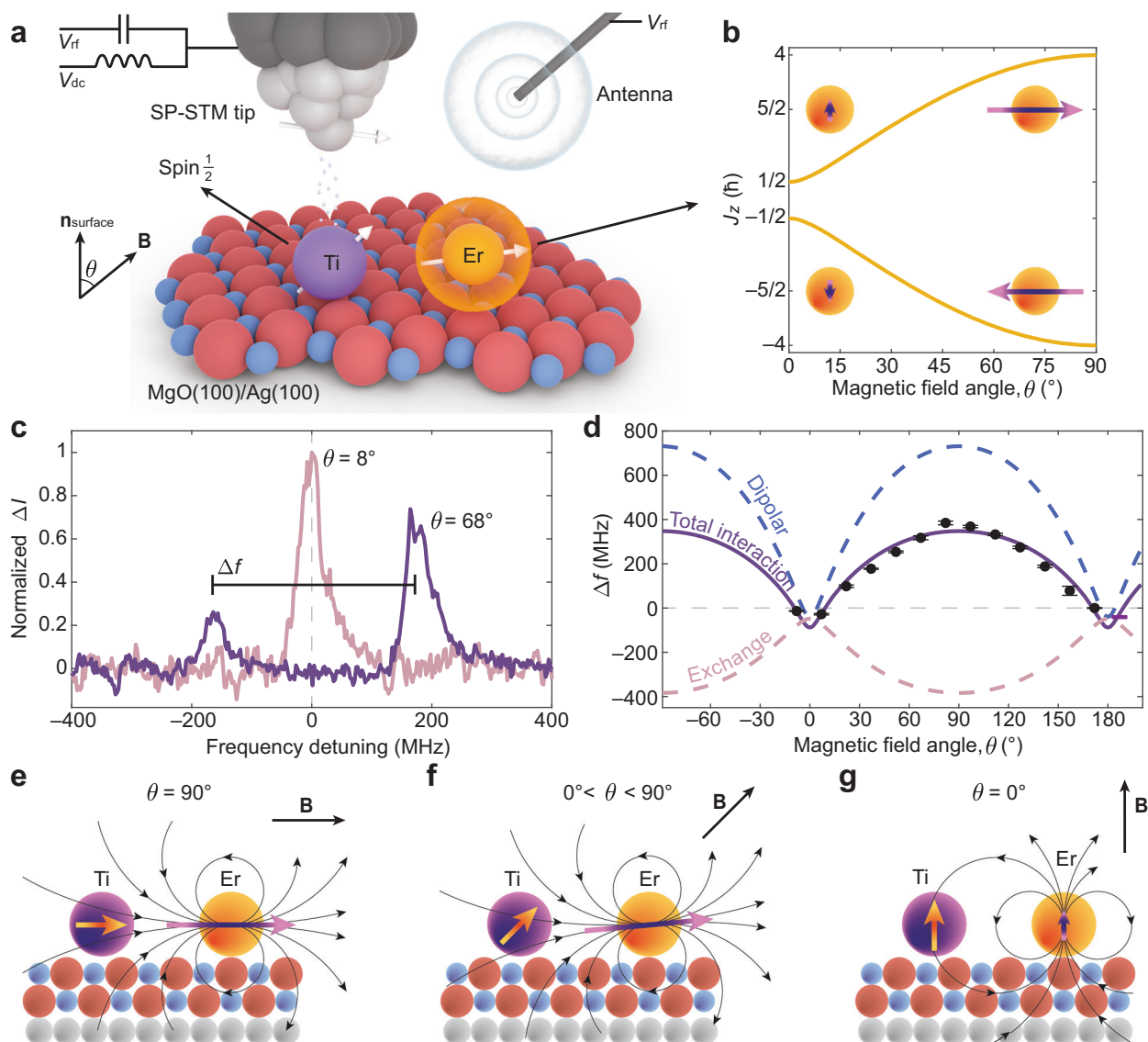


Fig. 1 | Probing Er 4f electron spins through a Ti spin sensor. **a** Schematic of the experimental set-up for ESR-STM measurement of an Er-Ti dimer built on MgO/Ag(100). The Ti atom (purple) is positioned close to the Er atom (orange) and located under a spin-polarized (SP) STM tip. The external magnetic field (\mathbf{B}) defines the z -direction and is applied at an angle ϑ from the out-of-plane direction. **b** Projected total angular momentum of Er (J_z) onto the \mathbf{B} field direction as a function of ϑ . The strong magnetic anisotropy favors an in-plane alignment of \mathbf{J}_{Er} . **c** ESR spectra of the Ti atom placed 0.928 nm apart from the Er atom at different ϑ . At $\vartheta = 8^\circ$, a single ESR peak is visible (pink) while, at $\vartheta = 68^\circ$ (purple), the two ESR peaks are separated due to the magnetic interactions between the Er and Ti. For the latter, the relative peak intensity indicates a ferromagnetic interaction (set-point: $V_{\text{dc}} = 50$ mV, $I_{\text{dc}} = 20$ pA, $V_{\text{rf}} = 12$ mV, $B = 0.3$ T). **d** ESR peak separation, Δf , as a

function of ϑ . The experimental points (black dots) were acquired at different set-points ($V_{\text{dc}} = 50$ mV, $I_{\text{dc}} = 12$ –30 pA, $V_{\text{rf}} = 12$ –20 mV, $B = 0.3$ T). We give error bars with 95% confidence interval. The total interaction (solid purple line) calculated by the model Hamiltonian is composed of a dipolar contribution (dashed blue line) and an exchange contribution (dashed pink line). **e–g** Schematic of the angular momenta of Er and Ti on MgO/Ag(100). The dipolar fields induced by Er are depicted as black curved arrows. When \mathbf{B} is applied along the in-plane direction ($\vartheta = 90^\circ$), the J_z is maximum and aligned with the spin of Ti giving the largest ferromagnetic dipolar interaction. When \mathbf{B} is rotated, the spin of Ti follows the direction of \mathbf{B} while the total angular momentum of Er is aligned preferentially in-plane (**f**). In the out-of-plane direction ($\vartheta = 0^\circ$), J_z is minimum and aligned with the spin of Ti (**g**) giving a small antiferromagnetic dipolar interaction.

efficient ESR driving. To characterize the magnetic states and anisotropy of Er, we utilized the dipole field sensing technique²⁸ with a Ti atom on the bridge binding site of MgO as a well-known spin sensor. On this binding site, Ti has a spin \mathbf{S}_{Ti} of magnitude $\hbar/2$ and a relatively weak g -factor anisotropy²⁹ compared to the oxygen binding site³⁰.

We deposited Er and Ti at cryogenic temperatures (~ 10 K) on 2 monolayers of MgO grown on Ag(100) (“Methods” section and Fig. S1a). Their binding sites on the surface can be changed by atom manipulation (Supplementary Section 2). When isolated, a nuclear spin-free Ti atom presents a single ESR signal under an external magnetic field (Fig. S3a). The ESR peak of Ti splits when coupled to an Er atom (Supplementary Section 4). Figure 1c shows the ESR spectra obtained on Ti in an Er-Ti dimer with the atomic separation of 0.928 nm (Fig. S2b). At the magnetic field of 0.3 T with $\vartheta = 8^\circ$, we observed one ESR peak at the resonance frequency of Ti, which splits into two peaks separated by $\Delta f = 334 \pm 3$ MHz when rotating \mathbf{B} close to the in-plane direction ($\vartheta = 68^\circ$). The two ESR peaks stem from the magnetic interaction with the Er spin fluctuating between two states²⁸ during the measurement, with the relative peak intensity being proportional to the time-averaged population of the Er states. The pronounced difference in the relative intensity of the ESR peaks indicates a large imbalance in the Er state occupation even at $B = 0.3$ T and 1.3 K, which reflects the large J_z of Er at $\vartheta = 68^\circ$ (Fig. 1b). The polarity of this asymmetry depends on the character of the magnetic interactions between the two atoms (Fig. S4b, e). In Fig. 1c, the peak at the lower frequency is less intense than the one at the higher frequency and, hence, the interaction can be regarded as ferromagnetic³¹, with this polarity defined as positive Δf in Fig. 1d. We observe changes in polarity at different field directions (Fig. 1d), indicating alternating couplings between ferromagnetic and antiferromagnetic states.

The angle dependence of Δf (Fig. 1d) gives a direct measurement of the Er-Ti interaction energy^{28,31} and of the magnetic anisotropy²³. To interpret it, we model the system through a spin-Hamiltonian including both the single atom Zeeman and anisotropy terms, as well as the interaction between the two spins:

$$H = \mu_B g_{\text{Er}} \mathbf{B} \cdot \mathbf{J}_{\text{Er}} + D J_{\perp}^2 + \mu_B \mathbf{B} \cdot \bar{g}_{\text{Ti}} \cdot \mathbf{S}_{\text{Ti}} + H_{\text{dip}} + H_{\text{exc}}. \quad (1)$$

Here, μ_B is the Bohr magneton, J_{\perp} is the out-of-plane component of \mathbf{J}_{Er} , $g_{\text{Er}} = 1.2$ is the Er Landé g -factor obtained from its atomic quantum numbers, and \bar{g}_{Ti} is the Ti anisotropic g -tensor²⁹. We use a magnetic anisotropy parameter $D = 2.4$ meV to match the Er energy splitting found in a previous study²³. The magnetic coupling consists of dipolar (H_{dip}) and Heisenberg exchange interactions (H_{exc}):

$$H_{\text{dip}} = \frac{\mu_0 \mu_B^2}{4\pi \hbar^2 r^3} [g_{\text{Er}} \mathbf{J}_{\text{Er}} \cdot \bar{g}_{\text{Ti}} \cdot \mathbf{S}_{\text{Ti}} - 3(\hat{\mathbf{r}} \cdot g_{\text{Er}} \mathbf{J}_{\text{Er}})(\hat{\mathbf{r}} \cdot \bar{g}_{\text{Ti}} \cdot \mathbf{S}_{\text{Ti}})], \quad (2)$$

$$H_{\text{exc}} = \frac{\mathcal{J}_{\text{exc}}}{\hbar^2} (\mathbf{J}_{\text{Er}} \cdot \mathbf{S}_{\text{Ti}}), \quad (3)$$

where μ_0 is the vacuum permittivity, r the separation between the two atoms, $\hat{\mathbf{r}}$ the unit vector connecting them²⁸, and \mathcal{J}_{exc} the exchange interaction energy expressed in terms of \mathbf{J}_{Er} ³². In our model, \mathcal{J}_{exc} is the only free parameter for the fit. As shown in Fig. 1d, our model accurately reproduces the data for $\mathcal{J}_{\text{exc}}/\hbar = 48$ MHz, where the positive sign indicates an antiferromagnetic coupling. This value is more than 20 times smaller than that observed for a Ti-Ti dimer at the same distance (1.16 GHz)³³. We ascribe the smaller Er-Ti coupling to the localization of the $4f$ orbitals near the atom’s core, which limits the overlap between Er and Ti orbitals when compared to the Ti-Ti case.

The strong angle dependence of Δf can be understood by considering the large magneto-crystalline anisotropy of \mathbf{J}_{Er} . At $\vartheta = 90^\circ$, J_z is at its maximum ($4\hbar$), and the angular momenta of both atoms are parallel to $\hat{\mathbf{r}}$ (Fig. 1e), which maximizes the contribution of the dipolar

coupling in a ferromagnetic configuration (positive Δf). When rotating \mathbf{B} away from the in-plane direction, \mathbf{S}_{Ti} follows the direction of \mathbf{B} , while the anisotropy of Er preserves a large component of \mathbf{J}_{Er} mainly aligned along the in-plane direction (Fig. 1f). This misalignment between the two angular momenta reduces the dipolar interaction. Finally, as \mathbf{B} approaches the surface normal (Fig. 1g), \mathbf{J}_{Er} turns towards the out-of-plane direction with a much smaller value of $J_z = \hbar/2$. With the two momenta being perpendicular to $\hat{\mathbf{r}}$, the dipolar interaction is antiferromagnetic (negative Δf). Conversely, the mutual projection of \mathbf{S}_{Ti} and \mathbf{J}_{Er} is the only factor modulating the exchange interaction term, which remains negative Δf (antiferromagnetic coupling with positive \mathcal{J}_{exc}) at all angles (dashed pink curve in Fig. 1d).

Spin resonance of Er 4f electrons

The direct drive of ESR in STM requires positioning the tip directly on top of the target atom¹⁹. However, despite using a tip showing ESR signal on an isolated Ti atom (Fig. S3a), we observed no ESR when positioning the tip over an Er atom (Fig. S3b), which we attribute to the small polarization of the $5d$ and $6s$ shells of Er and to the weak interaction between the $4f$ and tunneling electrons. The weak polarization of the outer shell is reflected in the absence of spin excitations in the dI/dV spectra (Fig. S1d, e, h). These factors were found to limit the tunneling magnetoresistance at the STM junction in other lanthanide atoms^{24,34}, possibly hindering both the ESR drive and detection²³.

To overcome this limitation, we built a strongly interacting Er-Ti dimer by positioning Ti at 0.72 nm from Er through atom manipulation (Fig. 2a and Supplementary Section 2). Similar to the isolated atom, we observed no ESR peaks at the Er position in the dimer (yellow curve in Fig. 2b). However, when the tip was positioned on Ti, we observed up to 5 peaks (pink and purple curves in Fig. 2b). The first two peaks below 10 GHz with $|\Delta f| = 2.70 \pm 0.01$ GHz correspond to the ESR transitions of Ti that were similarly found in the dimer with larger atomic separations (Fig. 1c). Hence, we label them as f_1^{Ti} and f_2^{Ti} , respectively. In this dimer, we observed that f_1^{Ti} shows a higher intensity than f_2^{Ti} , indicating an antiferromagnetic exchange interaction³¹ (Fig. S4c, f) dominating over the dipolar coupling at this atomic separation. At higher frequencies, we further observed two peaks that are significantly blue-shifted when rotating \mathbf{B} from $\vartheta = 52^\circ$ (pink curve in Fig. 2b) to 97° (purple). The higher resonance frequencies and pronounced angle dependence indicate that those transitions involve the large and anisotropic angular momentum of Er, and, thus, we label them as f_3^{Er} and f_4^{Er} . These transitions are not observed for all Er atoms, possibly due to the presence of isotopes with large nuclear spins for which the intensity of the ESR signal is spread over multiple peaks and is below the sensitivity of our measurements (Fig. S5). In addition, their frequency separation exactly matches the one between f_1^{Ti} and f_2^{Ti} , reflecting the same Er-Ti interaction. On the other hand, f_3^{Er} and f_4^{Er} are approximately equal in intensity, indicating that Ti fluctuates between two spin states with almost equal occupations. The comparable Ti states’ occupation stems from the scattering with tunneling electrons and from the Zeeman splitting of Ti (~ 7 GHz) being smaller than the thermal energy at the measurement temperature of 1.3 K (~ 27 GHz). With \mathbf{B} at $\vartheta = 52^\circ$, we observed one more peak at even higher frequencies. Its frequency exactly matches the sum of f_1^{Ti} and f_4^{Er} (or equivalently f_2^{Ti} and f_3^{Er}), which suggests an ESR transition involving both Ti and Er spins. We label this peak as f_5^{TiEr} . Remarkably, the sign of f_3^{Er} , f_4^{Er} and f_5^{TiEr} is opposite to that of f_1^{Ti} and f_2^{Ti} , indicating a different detection mechanism for the transitions involving the Er spin, which will be discussed below. Finally, we observed an energy level crossing between Er and Ti transitions at $\vartheta = 12^\circ$, with the Er resonance frequencies further shifting below the Ti transitions at $\vartheta = 0^\circ$ (Fig. 2c and Fig. S6). This peculiar behavior is a consequence of the large difference in magnetic anisotropy between Er and Ti²³.

As shown in Fig. 2c, the angular dependence of the ESR frequencies is well reproduced by using Eq. 1 with $\mathcal{J}_{\text{exc}}/\hbar = 326$ MHz for

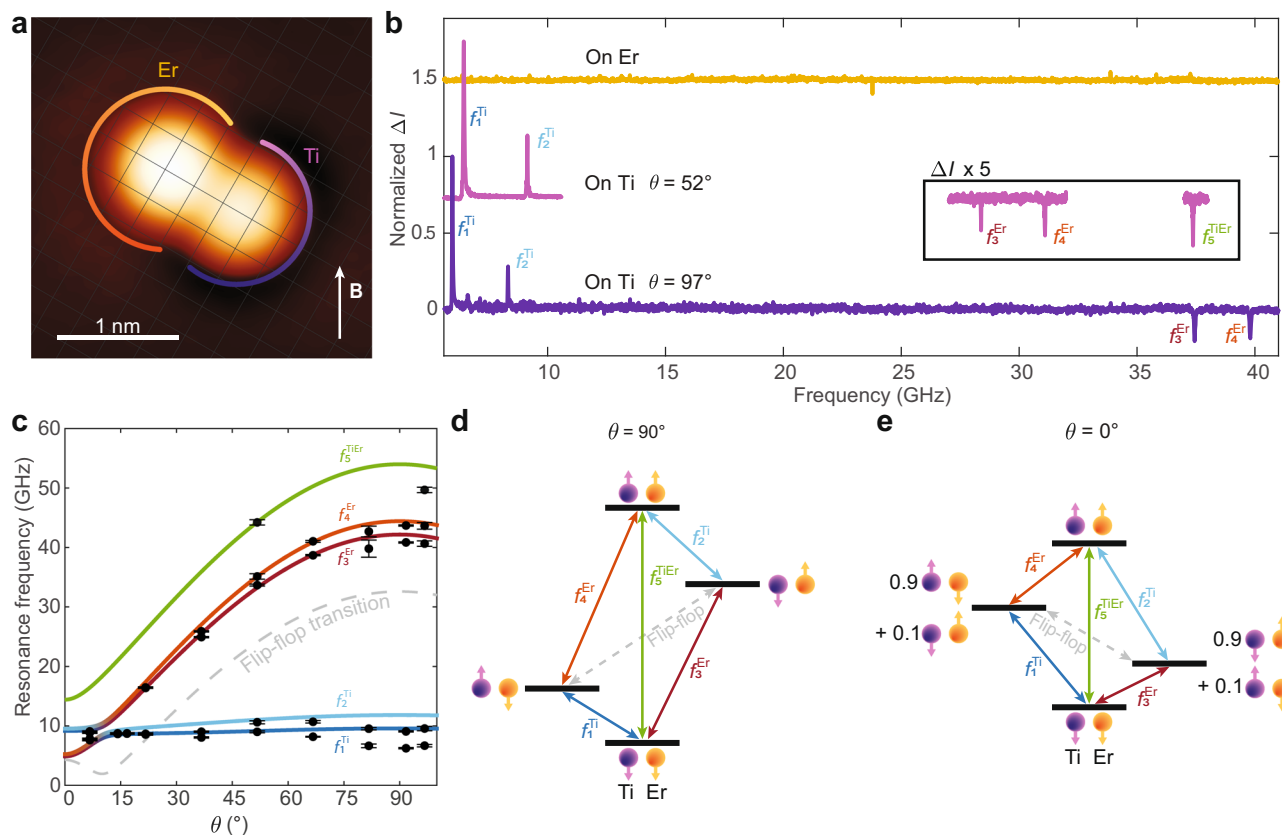


Fig. 2 | Measurement of Er ESR transitions through a strongly coupled Ti atom.

a Constant-current STM image of the engineered Er-Ti dimer with the atomic separation of 0.72 nm. The intersection of grids represents the oxygen sites of MgO. The Er atom (circled in yellow) is adsorbed on the oxygen site of MgO, while the Ti atom (circled in purple) is adsorbed on the bridge site (set-point: $V_{dc} = 100$ mV, $I_{dc} = 20$ pA). **b** ESR spectra of the dimer given in **a**. When the STM tip is located on top of Er, no peaks are observed (yellow) (set-point: $V_{dc} = 50$ mV, $I_{dc} = 20$ pA, $V_{rf} = 20$ mV, $B = 0.28$ T, $\vartheta = 97^\circ$). When the STM tip is located on top of Ti, 5 ESR peaks are detected (f_1^{Ti} , f_2^{Ti} , f_3^{Er} and f_4^{Er}) with $\vartheta = 52^\circ$ (pink), while 4 ESR peaks are detected (f_1^{Ti} , f_2^{Ti} , and f_3^{Er}) with $\vartheta = 97^\circ$ (purple) (set-point: $V_{dc} = 70$, 60 mV, $I_{dc} = 30$, 40 pA, $V_{rf} = 20$, 15 mV, $B = 0.3$ T). **c** ESR frequencies as a function of ϑ at $B = 0.32$ T. The

ESR frequencies obtained from each measurement are given as black dots with error bars with 95% confidence interval alongside the transition energies predicted from the model Hamiltonian for f_1^{Ti} (blue line), f_2^{Ti} (light blue line), f_3^{Er} (red line), f_4^{Er} (orange line), f_5^{TiEr} (green line), and flip-flop transition (dashed gray line). The experimental points were obtained at different set-points ($V_{dc} = 60$ –70 mV, $I_{dc} = 12$ –40 pA, $V_{rf} = 15$ –25 mV, $B = 0.28$ –0.8 T); the resonance frequencies were rescaled by 0.32 T/B. **d, e** Four-level schemes corresponding to the energies of the 4 spin states of the Er-Ti dimer and the corresponding transitions depicted as colored arrows at $B = 0.32$ T with different ϑ (90° and 0° , respectively). At $\vartheta = 90^\circ$ (**d**), the spin states are given by the Zeeman product states, while at $\vartheta = 0^\circ$ (**e**), a linear combination of the Zeeman product states is needed to describe the levels.

this Ti-Er pair with 0.72 nm separation. We observed small deviations for f_1^{Ti} , f_2^{Ti} and f_5^{TiEr} , which we ascribe to different experimental conditions and magnetic interaction of Ti with the tip, which is not included in our model. Diagonalizing the Hamiltonian in Eq. 1 allows us to analyze the quantum states of the Er-Ti dimer in terms of individual Er and Ti spin states. For an in-plane $B = 0.3$ T, the energy detuning between the Er and Ti spins (30 GHz) is much larger than the interaction energy (about 3 GHz). Therefore, the Er-Ti dimer can be modeled with the 4 Zeeman product states of the Er and Ti spins. Following this picture, we can support the assignment of $f_{1,2}^{Ti}$ as Ti spin transitions occurring with no changes in the Er state, while $f_{3,4}^{Er}$ correspond to Er spin transitions without altering Ti. Finally, we attribute f_5^{TiEr} to a double-flip transition involving both Er and Ti spins. Even though a $|\Delta m| > 1\hbar$ process is generally forbidden to first order, anisotropic terms in the magnetic interaction can give rise to higher order matrix elements connecting states with $\Delta m = \pm 2\hbar$ ³⁵.

When the field is oriented at $\vartheta = 0^\circ$, both \mathbf{J}_{Er} and \mathbf{S}_{Ti} show an expectation value of $\hbar/2$, but a detuning still occurs due to the difference between the out-of-plane g-factors, $g_{Er} = 1.2$ and $g_{Ti} = 1.989 \pm 0.024$ ²⁹. This detuning is comparable to their interaction energy and, thus, the two middle levels are no longer described by Zeeman product states (Fig. 2e). Finally, at the level crossing angle ($\vartheta \sim 12^\circ$), the two Er and Ti middle levels become singlet and triplet

states³³. However, measuring ESR spectra under these conditions becomes challenging (Fig. S7), possibly due to the limitation in our detection as discussed in the following.

Erbium ESR detection and driving mechanisms

The detection of ESR peaks exclusively occurs when the tip is positioned on top of Ti. Moving the tip from Ti to Er, the intensities of f_3^{Er} and f_4^{Er} gradually decrease and eventually vanish at ~ 0.3 nm from the Ti center (Fig. S8). This behavior indicates that driving an ESR transition on Er must induce a change in the Ti state occupation, subsequently modifying the spin polarization of the tunnel junction. In addition, while the Ti transitions always yield positive peaks $f_{1,2}^{Ti}$, Er ESR signals differ depending on specific tip conditions, i.e., different tips show positive or negative sign for $f_{3,4}^{Er}$ (Fig. 3a).

To further delve into the driving and detection mechanisms of the Er spin, we measured the intensities of f_1^{Ti} and f_3^{Er} as a function of V_{rf} using a tip that shows negative Er peaks (Fig. 3b). While f_1^{Ti} exhibits a continuous increase in intensity with increasing V_{rf} , f_3^{Er} reaches saturation at $V_{rf} \sim 20$ mV. The result for f_1^{Ti} aligns with previous measurements on Ti³³, while the low-power saturation of Er is comparable to that of Fe, which might reflect a long T_1 and/or a high Rabi rate (Ω)³⁶. To understand this V_{rf} -dependence as well as the signs of ESR signals, we developed a rate equation model (Supplementary Section 7) based

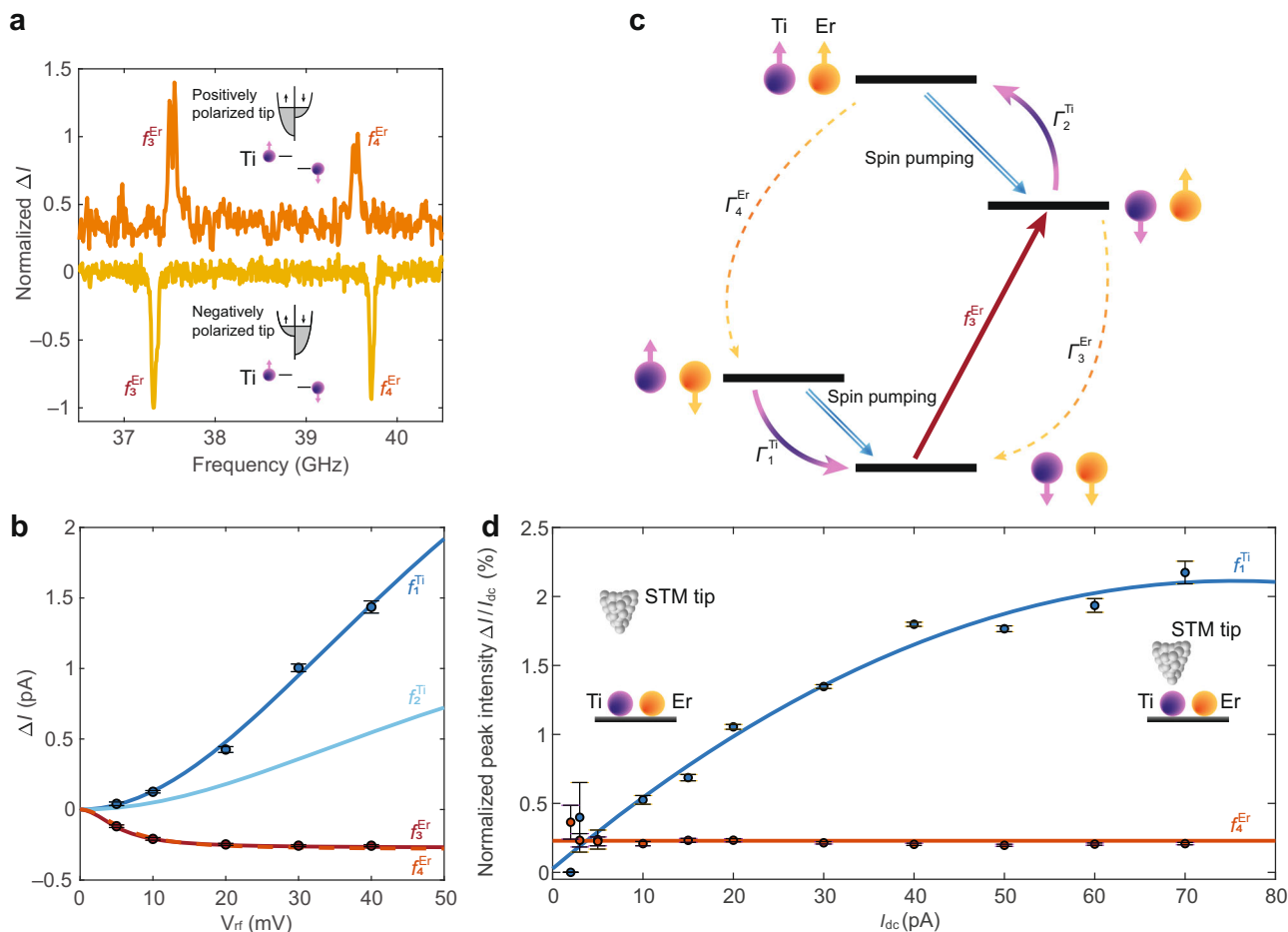


Fig. 3 | Detection and driving mechanisms of Er ESR transitions. **a** ESR spectra showing $f_{3,4}^{Er}$ for two different STM tips: negative peaks related to negative spin pumping (yellow line) and positive peaks related to positive spin pumping (orange line) (set-point: $I_{dc} = 12, 20$ pA, $V_{dc} = 70$ mV, $V_{rf} = 25$ mV, $B = 0.28, 0.32$ T, $\theta = 67^\circ$). **b** ESR peak intensities as a function of V_{rf} . The measured values for f_1^{Ti} and f_3^{Er} are given by black dots while the intensities predicted from the rate equation model (Supplementary Section 9) for $f_{1,2}^{Ti}$ and $f_{3,4}^{Er}$ are given as blue, light blue, red solid lines and an orange dashed line, respectively (set-point: $I_{dc} = 40$ pA, $V_{dc} = 70$ mV, $B = 0.28$ T, $\theta = 97^\circ$). **c** Four-level scheme explaining the rate equation model while

driving f_3^{Er} (red arrow). The Ti's spin relaxation rates Γ_1^{Ti} and Γ_2^{Ti} are depicted as purple arrows while the Er spin relaxation rates Γ_3^{Er} and Γ_4^{Er} are given as dashed yellow arrows. The negative spin pumping effect is represented as blue double arrows. **d** Normalized ESR peak intensities ($\Delta I / I_{dc}$) for f_1^{Ti} (blue circles) and for f_4^{Er} (orange circles) at different tip heights. Here, the tip height is controlled by the set-point current I_{dc} (set-point: $V_{dc} = 70$ mV, $V_{rf} = 10$ mV, $B = 0.28$ T, $\theta = 97^\circ$). The blue and orange lines serve as guides for the eye. The insets show two different tip-Ti distances: larger for lower I_{dc} and smaller for higher I_{dc} . In **b** and **d**, the error bars are given with 95% confidence interval.

on the four-level scheme depicted in Fig. 3c. When driving f_3^{Er} (red arrow), the populations of the initial and final states involved in the transition tend to equalize through a population transfer³⁷. The changes in population are counteracted by the relaxation rates of each state ($\Gamma_{1,2}^{Ti}$ and $\Gamma_{3,4}^{Er}$), which tend to repopulate the depleted states. These rates are inversely proportional to the T_1 of the atom involved in the spin flip. These relaxations happen due to an exchange of energy with the environment which tends to relax the populations towards the thermal equilibrium. An exchange of energy to (from) the environment leads to a transition to a lower (higher) energy level. Since Ti located under the tip is strongly influenced by tunneling electrons, relaxation events occur on a much shorter timescale than for Er³⁸, providing a more efficient pathway to attain the steady state. In addition, to account for the tip-dependent sign and intensity of Er ESR signals, we included a spin pumping term originating from the spin-polarized tunnel current (Fig. 3c for a negatively polarized tip)^{17,39}. In inelastic scattering events, the exchange of angular momenta occurs while retaining the total angular momentum of the system³⁹. That is, the spin-polarized tunneling electrons lead to scattering events with preferential polarization, as depicted in the inset of Fig. 3a, c. Thus, the tunneling electrons can shift the Ti spin occupation altering the population balance with

respect to the thermal equilibrium (see Supplementary Section 9). The proposed detection scheme based on the change of Ti state population accurately describes the V_{rf} -dependence (Fig. 3b) and the tip-dependent sign variations of the ESR signals (Fig. S10b).

Finally, to identify the ESR driving source of the Er spin, we follow the relative peak intensity ($\Delta I / I_{dc}$) at different tip heights, as controlled by I_{dc} . As shown in Fig. 3d, $\Delta I / I_{dc}$ of f_1^{Ti} increases with reducing the tip-sample distance (increasing I_{dc}), indicating that the main driving term for Ti arises from the exchange interaction with the spin-polarized tip^{40,41}. On the other hand, $\Delta I / I_{dc}$ for f_4^{Er} remains independent of I_{dc} , which identifies the modulation of the magnetic interaction with Ti as the ESR driving source of Er⁴². The modulation of the magnetic coupling⁴³, in combination with anisotropic interaction terms³⁵, additionally explains the drive of the double-flip transition f_5^{TiEr} .

Relaxation time measurement through electron-electron double resonance

As previously discussed about the Er-Ti dimer with 0.928 nm separation, the relative peak intensity of the Ti peaks f_1^{Ti} and f_2^{Ti} reflects the time averaged population of the Er states (Fig. 4a), i.e., changes in the time-averaged spin states of Er will induce the change of the relative peak

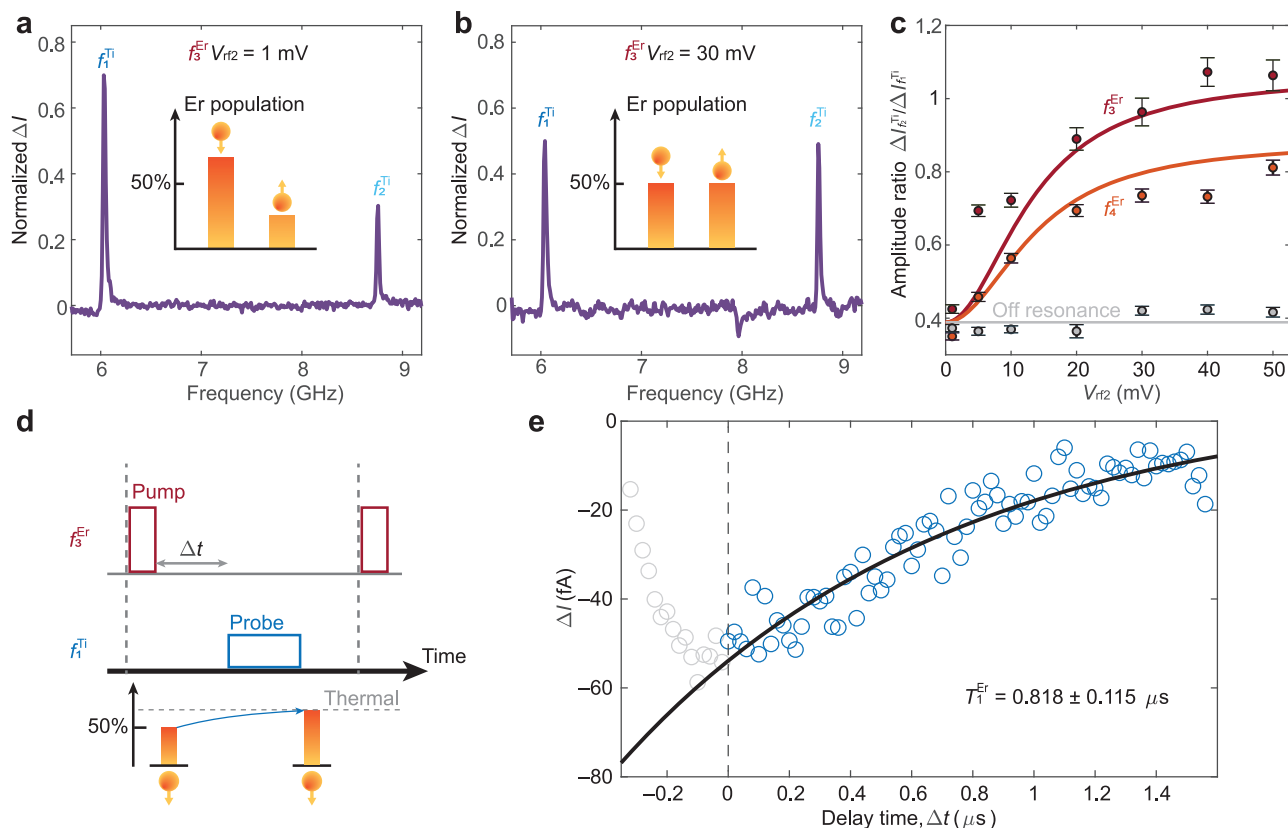


Fig. 4 | Determination of Er spin relaxation time. **a, b** Double resonance spectra in the frequency range covering Ti ESR transitions $f_{1,2}^{\text{Ti}}$ (**a**) without and (**b**) with simultaneous driving of Er at the ESR frequency of f_3^{Er} . The peak intensities of $f_{1,2}^{\text{Ti}}$ are related to the relative population of the Er spin states (insets). The spectra were normalized to the sum of their peak intensity. **c** ESR intensity ratios between $\Delta I_{f_2}^{\text{Ti}}$ and $\Delta I_{f_1}^{\text{Ti}}$ as a function of the driving strength $V_{\text{rf}2}$ at different Er ESR transition states (red, orange, and gray circles for f_3^{Er} , f_4^{Er} , and off-resonance, respectively). The solid curves show the correspondent simulation results by the rate equation model (Supplementary Section 9) for f_3^{Er} (red line), f_4^{Er} (orange line) and at an off-resonance frequency (gray line). The experimental points are given as black dots with error bars corresponding to 95% confidence interval. Set-point: $I_{\text{dc}} = 15$ pA,

$V_{\text{dc}} = 70$ mV, $V_{\text{rf}} = 30$ mV, $V_{\text{rf}2} = 1\text{--}50$ mV, $B = 0.28$ T, $\theta = 97^\circ$. **d** Schematics of the inversion recovery measurement in a pump-probe pulse scheme to determine the Er spin relaxation time T_1^{Er} . Each sequence is composed of a pump pulse at the resonance frequency of f_3^{Er} (red box) and a probe pulse at the resonance frequency of f_1^{Ti} (blue box). The probe pulse follows the pump pulse after a delay time Δt . The population of the Er states after the pump pulse relaxes back to the thermal state following its T_1 . **e** The experimental data for the inversion recovery measurement (blue circles) show the intensity of the ESR signal at the probe pulse f_1^{Ti} as a function of Δt . The black line shows the fit using an exponential function with T_1^{Er} of about 1 μs . Set-point: $I_{\text{dc}} = 50$ pA, $V_{\text{dc}} = 70$ mV, $V_{\text{rf pump}} = 60$ mV, $V_{\text{rf probe}} = 100$ mV, $B = 0.28$ T, $\theta = 97^\circ$.

intensity of f_1^{Ti} and f_2^{Ti} . Thus, by monitoring the Ti ESR signals, we can observe the evolution of the Er spin state. In this way, we characterize the characteristic relaxation time T_1^{Er} by exciting the Er into an out-of-equilibrium state and monitoring its relaxation towards the thermal state.

By applying an additional rf voltage ($V_{\text{rf}2}$), Ti and Er spins can be simultaneously driven in the so-called “electron-electron double resonance” scheme⁴⁴. With this scheme, it is possible to drive Er transitions and sense the change in population through the Ti ones. For instance, in double resonance experiment, the relative intensities of f_1^{Ti} and f_2^{Ti} are equalized when f_3^{Er} is simultaneously driven (Fig. 4b). As shown in Fig. 4c, the intensity ratio of f_1^{Ti} and f_2^{Ti} ($\Delta I_{f_2}^{\text{Ti}}/\Delta I_{f_1}^{\text{Ti}}$) increases with increasing V_{rf} only when $V_{\text{rf}2}$ is applied at the resonance frequency of f_3^{Er} or f_4^{Er} , enabling selective modulation of the Er states to an out-of-equilibrium configuration.

Taking advantage of this selective driving mechanism, we implemented an inversion recovery measurement to estimate the spin relaxation time of Er (T_1^{Er}) in a pump-probe scheme (Fig. 4d). After exciting f_3^{Er} with a pumping rf pulse of 200 ns duration that equalized the Er population, we applied a probe pulse of 500 ns for f_1^{Ti} after a delay time Δt . Using this sequence, we monitored the time evolution of the intensity of f_1^{Ti} as a function of Δt from the out-of-equilibrium to the thermal state (Fig. 4e). The fit to an exponential function (Fig. 4e) gives $T_1^{\text{Er}} = 0.818 \pm 0.115$ μs , which is five times longer than that

previously measured for Fe-Ti dimers in the absence of tunnel current¹⁸. We attribute this enhancement to the efficient decoupling of 4f electrons from the environment, which reduces the relaxation events arising from the scattering with substrate electrons.

The T_1^{Er} observed through Ti likely differs from the intrinsic relaxation time of Er on this surface due to its strong interaction with the Ti atom. Nevertheless, the large T_1^{Er} indicates that the rapid spin fluctuations of Ti occurring on the timescale of a few ns³⁸ do not significantly perturb the stability of the Er states. This property partially originates from the large energy detuning between Er and Ti levels, which prevents the energy exchange required for spin-flip events. Using the experimentally obtained value of T_1^{Er} in the rate equation model, we extract a driving term $W = \Omega^2 T_2/2$ for Er that is two times larger than for Ti in the same dimer (Supplementary Section 9). Despite the long spin lifetime and large driving term, attempts to drive Er Rabi oscillations through Ti do not yield a complete cycle (Fig. S11b), preventing a direct measure of the Er T_2 . This is most likely due to a relatively low Rabi rate Ω provided by the moderate Er-Ti exchange coupling, which is about 2–3 times smaller than in the Fe-Ti dimer⁴². In turn, a low value of Ω together with a large driving term W would imply much longer T_2 for Er than previous 3d elements, highlighting the potential of 4f electrons to realize higher performance atomic-scale qubits.

Discussion

We demonstrated a new experimental approach to electrically drive ESR on the elusive $4f$ electrons in a surface-adsorbed lanthanide atom with long spin relaxation time. Given the reduced scattering with the substrate electrons, it is reasonable to anticipate an enhancement in the coherence time of Er in comparison to $3d$ elements. This allows one to develop more advanced pulse sequences for quantum coherent manipulation on atomic-scale spin platforms. We expect that, by employing a similar approach to different atomic structures, we can reduce the influence of the spin fluctuations of the atom used for the detection and amplify the ESR driving on the $4f$ electrons, enabling the use of lanthanide atoms as surface spin qubits with superior properties compared to the routinely adopted $3d$ elements.

Methods

STM measurements

Our experiment was performed in a home-built STM operating at the cryogenic temperature of -1.3 K in an ultrahigh vacuum environment ($<1 \times 10^{-9}$ Torr)⁴⁵. Using a two-axis vector magnet (6 T in-plane/4 T out-of-plane), the magnetic fields were varied from 0.28 T to 0.9 T at different angles from the surface normal⁴⁵. To allow atom deposition on the sample kept in the STM stage, the sample is slightly tilted from the axis of the magnet by -7° as estimated from the fit to the data shown in Fig. 1d. Considering this misalignment, all our experimental ϑ were offset by that amount accordingly. The magnetic tips used in our measurements were prepared by picking up -4 – 9 Fe atoms from the MgO surface until the tips presented good ESR signals on isolated Ti atoms.

ESR measurements

We used two different schemes to apply V_{rf} to the STM junction: one through the tip and one through an antenna (rf generators: Keysight E8257D and E8267D)⁴⁵. In all our measurement involving a single rf sweep, we applied the V_{rf} using an antenna located near the sample⁴⁵ except for the data in Fig. 3b, where the V_{rf} was combined with the dc bias voltage V_{dc} using a bias tee at room temperature and then applied to the STM tip. The data in Fig. 4a–c were acquired by applying V_{rf} to the tip and simultaneously V_{rf2} to the antenna. For the measurements reported in Figs. 4e and S11, the two rf voltages (V_{rf} and V_{rf2}) were combined through a power splitter (minicircuits ZC2PD-K0244+) and applied to the STM tip. For these measurements, both rf generators were gated by an arbitrary waveform generator (Tektronix, AWG 70002B).

Sample preparation

The surface of a Ag(100) substrate was cleaned by repeated cycles of Ar⁺ sputtering and annealing (700 K). We grew atomically thin layers of MgO(100) on the Ag(100) by evaporating Mg metal in an oxygen atmosphere with partial pressure of 10^{-6} Torr while maintaining the sample at a temperature of -590 K, following a procedure described in a previous work⁴⁶. We deposited Fe, Ti and Er atoms ($<1\%$ of monolayer) from high purity rods ($>99\%$) using an e-beam evaporator. During the deposition the sample was held at -10 K in order to have well-isolated single atoms on the surface. As described in previous works, the Ti atoms on 2 ML MgO/Ag(100) show a spin magnitude of $\hbar/2$ with g-factor anisotropy²⁹, a behavior previously attributed to hydrogenation³¹.

Analysis of ESR spectra

We fit the ESR spectra using a model given in³³ in order to extract the resonance frequency, peak intensity, and peak width for the data shown in Figs. 1d, 2c, 3b, d, and 4c.

ESR spectra normalization

Figure 1c: The spectrum at $\vartheta = 8^\circ$ (pink) was normalized at its maximum intensity, while the spectrum at $\vartheta = 68^\circ$ (purple) was normalized to the sum of the intensities of its two peaks. The frequency detuning is

defined with respect to 9.1 GHz (8.1 GHz) for the spectrum at $\vartheta = 8^\circ$ ($\vartheta = 68^\circ$).

Figure 2b: The spectra measured on Ti at $\vartheta = 52^\circ$ (pink) and at $\vartheta = 97^\circ$ (purple) were normalized at their respective maxima, while the spectrum measured on top of Er was rescaled by the same amount used for the spectrum measured on Ti at $\vartheta = 97^\circ$. The spectra measured on Ti at $\vartheta = 52^\circ$ and on Er are offset for clarity.

Reporting summary

Further information on research design is available in the Nature Portfolio Reporting Summary linked to this article.

Data availability

The data used in this study are available in the figshare database under accession code [<https://doi.org/10.6084/m9.figshare.24190884>].

Code availability

The code used to plot Figs. 1d, 2c, 3b, and 4c are available alongside the relative data at <https://doi.org/10.24433/CO.9869055.v1>.

References

- Heinrich, A. J. et al. Quantum-coherent nanoscience. *Nat. Nanotechnol.* **16**, 1318–1329 (2021).
- Donati, F. et al. Magnetic remanence in single atoms. *Science* **352**, 318–321 (2016).
- Dey, A., Kalita, P. & Chandrasekhar, V. Lanthanide(III)-based single-ion magnets. *ACS Omega* **3**, 9462–9475 (2018).
- Pedersen, K. S. et al. Toward molecular $4f$ single-ion magnet qubits. *J. Am. Chem. Soc.* **138**, 5801–5804 (2016).
- Shiddiq, M. et al. Enhancing coherence in molecular spin qubits via atomic clock transitions. *Nature* **531**, 348 (2016).
- Vincent, R., Klyatskaya, S., Ruben, M., Wernsdorfer, W. & Balestro, F. Electronic read-out of a single nuclear spin using a molecular spin transistor. *Nature* **488**, 357–360 (2012).
- Thiele, S. et al. Electrically driven nuclear spin resonance in single-molecule magnets. *Science* **344**, 1135–1138 (2014).
- Macfarlane, R. M. High-resolution laser spectroscopy of rare-earth doped insulators: a personal perspective. *J. Lumin.* **100**, 1–20 (2002).
- Serrano, D. et al. Ultra-narrow optical linewidths in rare-earth molecular crystals. *Nature* **603**, 241–246 (2022).
- Rančić, M., Hedges, M. P., Ahlfeldt, R. L. & Sellars, M. J. Coherence time of over a second in a telecom-compatible quantum memory storage material. *Nat. Phys.* **14**, 50–54 (2017).
- Zhong, T. et al. Optically addressing single rare-earth ions in a nanophotonic cavity. *Phys. Rev. Lett.* **121**, 183603 (2018).
- Kolesov, R. et al. Optical detection of a single rare-earth ion in a crystal. *Nat. Commun.* **3**, 1029 (2012).
- Kindem, J. M. et al. Control and single-shot readout of an ion embedded in a nanophotonic cavity. *Nature* **580**, 201–204 (2020).
- Yin, C. et al. Optical addressing of an individual erbium ion in silicon. *Nature* **497**, 91–94 (2013).
- Meier, F., Zhou, L., Wiebe, J. & Wiesendanger, R. Revealing magnetic interactions from single-atom magnetization curves. *Science* **320**, 82–86 (2008).
- Franke, K. J., Schulze, G. & Pascual, J. I. Competition of superconducting phenomena and kondo screening at the nanoscale. *Science* **332**, 940–944 (2011).
- Khajetoorians, A. A. et al. Current-driven spin dynamics of artificially constructed quantum magnets. *Science* **339**, 55–59 (2013).
- Wang, Y. et al. An atomic-scale multi-qubit platform. *Science* **382**, 87–92 (2023).
- Baumann, S. et al. Electron paramagnetic resonance of individual atoms on a surface. *Science* **350**, 417–420 (2015).

20. Seifert, T. S., Kovarik, S., Gambardella, P. & Stepanow, S. Accurate measurement of atomic magnetic moments by minimizing the tip magnetic field in STM-based electron paramagnetic resonance. *Phys. Rev. Res.* **3**, 043185 (2021).
21. Drost, R. et al. Combining electron spin resonance spectroscopy with scanning tunneling microscopy at high magnetic fields. *Rev. Sci. Instrum.* **93**, 043705 (2022).
22. Chen, Y., Bae, Y. & Heinrich, A. J. Harnessing the quantum behavior of spins on surfaces. *Adv. Mater.* **35**, 2107534 (2022).
23. Reale, S. et al. Erbium and thulium on MgO(100)/Ag(100) as candidates for single atom qubits. *Phys. Rev. B* **107**, 045427 (2023).
24. Singha, A. et al. Engineering atomic-scale magnetic fields by dysprosium single atom magnets. *Nat. Commun.* **12**, 4179 (2021).
25. Donati, F. et al. Correlation between electronic configuration and magnetic stability in dysprosium single atom magnets. *Nano Lett.* **21**, 8266–8273 (2021).
26. Natterer, F. D., Donati, F., Patthey, F. & Brune, H. Thermal and magnetic-field stability of holmium single-atom magnets. *Phys. Rev. Lett.* **121**, 027201 (2018).
27. Forrester, P. R. et al. Quantum state manipulation of single atom magnets using the hyperfine interaction. *Phys. Rev. B* **100**, 180405 (2019).
28. Choi, T. et al. Atomic-scale sensing of the magnetic dipolar field from single atoms. *Nat. Nanotechnol.* **12**, 420–424 (2017).
29. Kim, J. et al. Spin resonance amplitude and frequency of a single atom on a surface in a vector magnetic field. *Phys. Rev. B* **104**, 174408 (2021).
30. Steinbrecher, M. et al. Quantifying the interplay between fine structure and geometry of an individual molecule on a surface. *Phys. Rev. B* **103**, 155405 (2021).
31. Yang, K. et al. Engineering the Eigenstates of coupled spin-1/2 atoms on a surface. *Phys. Rev. Lett.* **119**, 227206 (2017).
32. Vieru, V., Iwahara, N., Ungur, L. & Chibotaru, L. F. Giant exchange interaction in mixed lanthanides. *Sci. Rep.* **6**, 24046 (2016).
33. Bae, Y. et al. Enhanced quantum coherence in exchange coupled spins via singlet-triplet transitions. *Sci. Adv.* **4**, eaau4159 (2018).
34. Natterer, F. D. et al. Reading and writing single-atom magnets. *Nature* **543**, 226 (2017).
35. Sadiq, G., Lashin, E. I. & Abdalla, M. S. Entanglement of a two-qubit system with anisotropic XYZ exchange coupling in a nonuniform time-dependent external magnetic field. *Phys. B: Condens. Matter* **404**, 1719–1728 (2009).
36. Willke, P. et al. Tuning single-atom electron spin resonance in a vector magnetic field. *Nano Lett.* **19**, 8201–8206 (2019).
37. Willke, P. et al. Probing quantum coherence in single-atom electron spin resonance. *Sci. Adv.* **4**, eaq1543 (2018).
38. Seifert, T. S. et al. Longitudinal and transverse electron paramagnetic resonance in a scanning tunneling microscope. *Sci. Adv.* **6**, eabc5511 (2020).
39. Loth, S. et al. Controlling the state of quantum spins with electric currents. *Nat. Phys.* **6**, 340–344 (2010).
40. Lado, J. L., Ferrón, A. & Fernández-Rossier, J. Exchange mechanism for electron paramagnetic resonance of individual adatoms. *Phys. Rev. B* **96**, 205420 (2017).
41. Reina-Gálvez, J., Wolf, C. & Lorente, N. Many-body nonequilibrium effects in all-electric electron spin resonance. *Phys. Rev. B* **107**, 235404 (2023).
42. Phark, S.-h et al. Electric-field-driven spin resonance by on-surface exchange coupling to a single-atom magnet. *Adv. Sci.* **n/a**, 2302033 (2023).
43. Niskanen, A. O. et al. Quantum coherent tunable coupling of superconducting qubits. *Science* **316**, 723–726 (2007).
44. Phark, S.-h et al. Double-resonance spectroscopy of coupled electron spins on a surface. *ACS Nano* **17**, 14144–14151 (2023).
45. Hwang, J. et al. Development of a scanning tunneling microscope for variable temperature electron spin resonance. *Rev. Sci. Instrum.* **93**, 093703 (2022).
46. Paul, W. et al. Control of the millisecond spin lifetime of an electrically probed atom. *Nat. Phys.* **13**, 403–407 (2017).

Acknowledgements

We thank Taehong Ahn and Leonard Edens for their support at the initial stage of the experiment and Yi Chen, Arzhang Ardavan, and Joaquín Fernández-Rossier for fruitful discussions. We acknowledge support from the Institute for Basic Science (IBS-R027-D1). Y.B. acknowledges support from Asian Office of Aerospace Research and Development (FA2386-20-1-4052). H.B. acknowledges funding from the SNSF AdG (TMAG-2_209266).

Author contributions

S.R. and F.D. conceived the idea. S.R., F.D., and Y.B. designed the experiment. S.R., J.H., J.O., and Y.B. performed the experiments. S.R. analyzed the data and developed the model with the supervision of F.D. and Y.B.; H.B., A.J.H., F.D., and Y.B. supervised the project. S.R., F.D., and Y.B. wrote the manuscript with contributions from all authors. All authors discussed the results.

Competing interests

The authors declare no competing interests.

Additional information

Supplementary information The online version contains supplementary material available at <https://doi.org/10.1038/s41467-024-49447-y>.

Correspondence and requests for materials should be addressed to Fabio Donati or Yujeong Bae.

Peer review information *Nature Communications* thanks the anonymous reviewers for their contribution to the peer review of this work. A peer review file is available.

Reprints and permissions information is available at <http://www.nature.com/reprints>

Publisher's note Springer Nature remains neutral with regard to jurisdictional claims in published maps and institutional affiliations.

Open Access This article is licensed under a Creative Commons Attribution 4.0 International License, which permits use, sharing, adaptation, distribution and reproduction in any medium or format, as long as you give appropriate credit to the original author(s) and the source, provide a link to the Creative Commons licence, and indicate if changes were made. The images or other third party material in this article are included in the article's Creative Commons licence, unless indicated otherwise in a credit line to the material. If material is not included in the article's Creative Commons licence and your intended use is not permitted by statutory regulation or exceeds the permitted use, you will need to obtain permission directly from the copyright holder. To view a copy of this licence, visit <http://creativecommons.org/licenses/by/4.0/>.

© The Author(s) 2024

Supplementary Information

Electrically Driven Spin Resonance of 4f Electrons in a Single Atom on a Surface

Stefano Reale^{1,2,3}, Jiyeon Hwang^{1,4}, Jeongmin Oh^{1,4}, Harald Brune⁵, Andreas J. Heinrich^{1,4}, Fabio Donati^{1,4*}, and Yujeong Bae^{1,4*†}

¹ Center for Quantum Nanoscience (QNS), Institute for Basic Science (IBS), Seoul 03760, Republic of Korea

² Ewha Womans University, Seoul 03760, Republic of Korea

³ Department of Energy, Politecnico di Milano, Milano 20133, Italy

⁴ Department of Physics, Ewha Womans University, Seoul 03760, Republic of Korea

⁵ Institute of Physics, Ecole Polytechnique Fédérale de Lausanne, 1015 Lausanne, Switzerland

*Corresponding authors: F.D. (donati.fabio@qns.science), Y.B. (bae.yujeong@qns.science)

†Current address: Empa, Swiss Federal Laboratories for Materials Science and Technology, nanotech@surfaces Laboratory, 8600, Dübendorf, Switzerland

Table of contents

- 1- Experimental set-up and identification of atomic species
- 2- Atom manipulation to construct Er-Ti dimers
- 3- Electron spin resonance on isolated Ti and Er
- 4- Effect of the Er-Ti coupling on the ESR spectra of Ti
- 5- Dimer with ¹⁶⁷Er
- 6- Tip position dependence of ESR signals on the Er-Ti dimer
- 7- Electron spin resonance spectra with out-of-plane magnetic fields
- 8- Electron spin resonance spectra around the energy level crossing
- 9- Rate equation model
- 10- Measurement of Rabi oscillations

1- Experimental set-up and identification of atomic species

From the STM image in Fig. S1a, it is possible to distinguish the MgO(100) patch from the Ag(100) substrate by the different apparent height. On top of the MgO patch, different atoms are distinguishable by their distinct apparent heights: ~130 pm for Ti on the oxygen site (Ti_O), ~210 pm for Ti on the bridge site (Ti_B), ~210 pm for Er on the oxygen site (Er_O), ~285 pm for Er on the bridge site (Er_B), and ~170 pm for Fe on the oxygen site as measured at $V_{dc} = 100$ mV. The species are further identified by their dI/dV spectra (Fig. S1b–k). While most of the atoms are distinguishable from the apparent heights and the spectral features, the Er_O and Ti_B present a similar apparent height as well as no clear spectral features. To distinguish these two species, we utilize the spin-polarized STM tip. In contrast with Er_O (Fig. S1h), the dI/dV spectrum measured on Ti_B using the spin-polarized STM tip (Fig. S1g) presents a step-like feature characteristic of a

spin-flip excitation at around zero bias¹ similarly to Ti_O (Fig. S1f). In the main text and in the following sections, we simply refer to Ti_B as Ti and Er_O as Er.

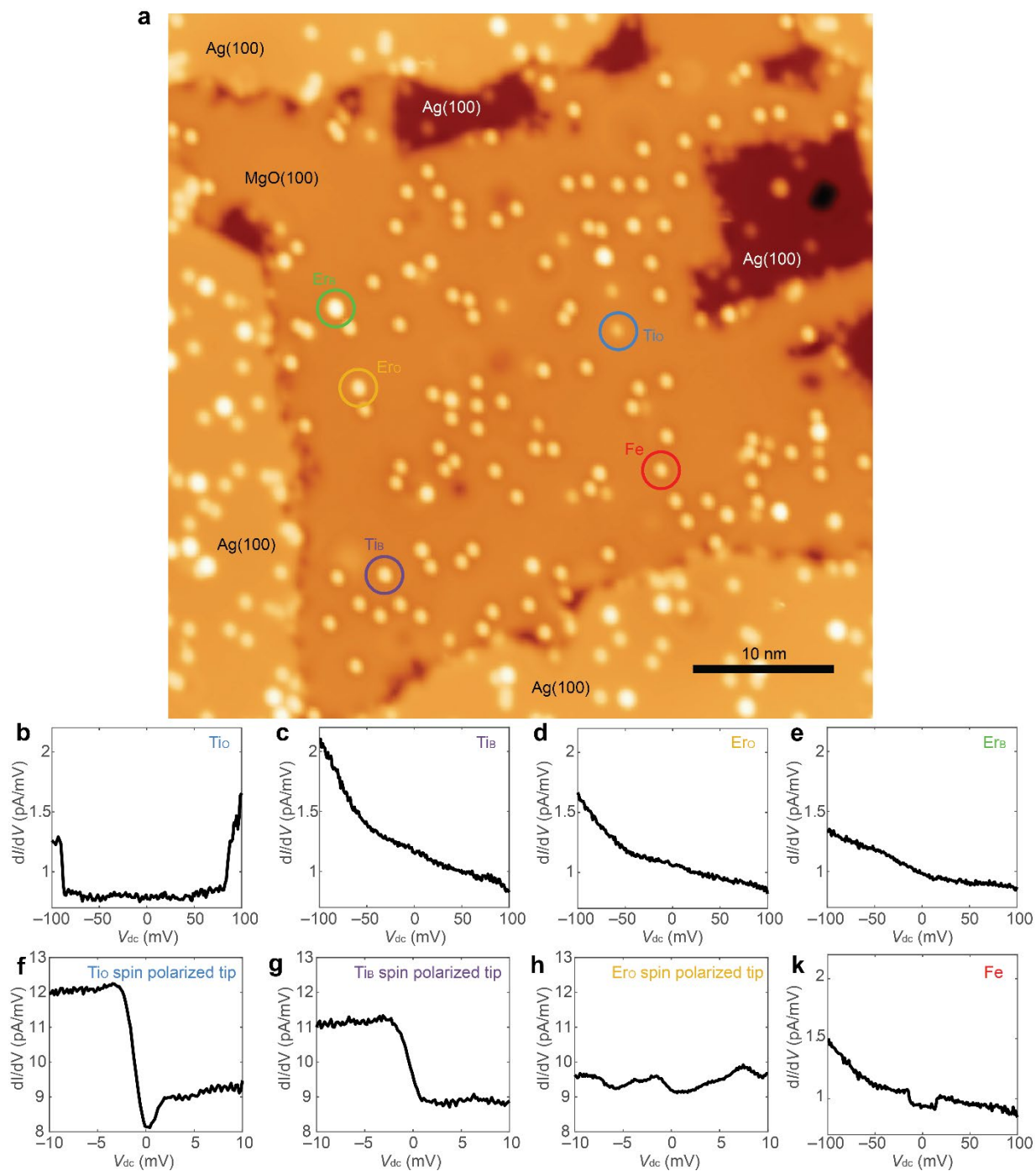


Figure S1 | Characterization of the atomic species. **a**, Constant current STM image of the Ag(100) surface partially covered by two-monolayers of MgO(100) (set point: $V_{dc} = 100$ mV, $I_{dc} = 20$ pA). The different atomic species can be distinguished by their apparent heights and dI/dV features: **(b)** Ti on the oxygen site (Ti_O), **(c)** Ti on the bridge site (Ti_B), **(d)** Er on the oxygen site (Er_O), **(e)** Er on the bridge site (Er_B), and **(k)** Fe. **(f)** Ti_O and **(g)** Ti_B present a spin-flip excitation at around 0 mV when measured with a spin polarized tip, while no excitation is present on Er_O **(h)**.

2- Atom manipulation to construct Er-Ti dimers

The Er-Ti dimer used to acquire the data presented in Fig. 1c,d was built through atom manipulation. After identifying a Ti atom and an Er atom, we manipulated the Ti adsorption site by the following procedure: 1) position the STM tip one lattice site away from the Ti center (set point: $V_{dc} = 100$ mV, $I_{dc} = 20$ pA), 2) switch off the STM feedback, 3) approach the tip by 330 pm to the surface, 4) apply a voltage pulse of 330 mV, and 5) switch the feedback on. This procedure allows us to move the Ti atom by half lattice sites (from Ti_o to Ti_b and vice versa) in a controlled manner. We repeated this procedure until we obtained the desired Er-Ti dimer with a distance of 0.928 nm (Fig. S2) with the Ti atom placed at the (-2, 2.5) lattice position from Er. We used a similar procedure to prepare the Er-Ti dimers with 0.72 nm separation with the Ti atom placed at the ($\pm 2.5, 0$) or ($0, \pm 2.5$) lattice position from Er.

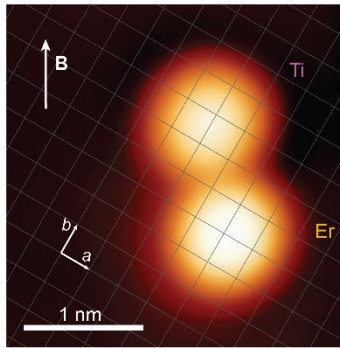


Figure S2 | Constant-current STM image of the Er-Ti dimer with 0.928 nm separation (set point: $V_{dc} = 100$ mV, $I_{dc} = 20$ pA). The intersection of grids represents the oxygen site of MgO and the lattice vectors (a, b) are superimposed on the grid.

3- Electron spin resonance on isolated Ti and Er

In order to perform ESR on an isolated Er atom, we confirmed whether the prepared spin-polarized tip is suitable to perform ESR or not, by measuring the ESR signal on an isolated Ti atom (Fig. S3a). When positioning the same tip over an isolated Er atom, however, no ESR peak was detectable (Fig. S3b).

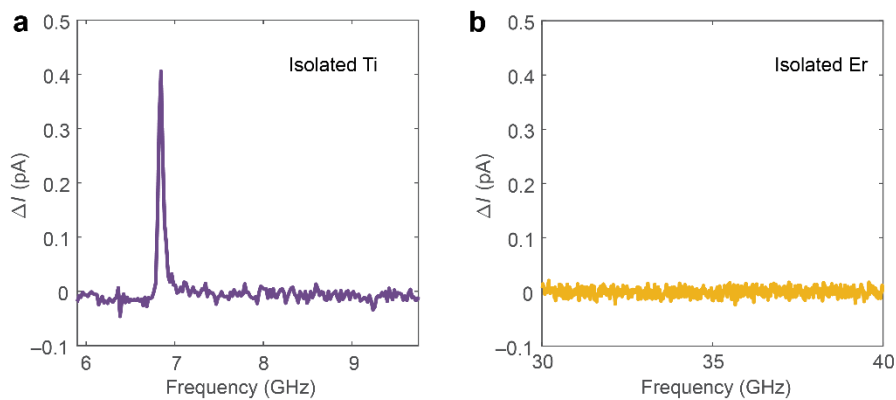


Figure S3 | Electron spin resonances on the isolated atoms. **a**, ESR spectrum measured with the STM tip positioned above an isolated Ti atom (set point: $V_{dc} = 60$ mV, $I_{dc} = 20$ pA, $V_{rf} = 20$ mV, $B = 0.28$ T, $\theta = 97^\circ$). **b**, ESR spectrum measured with the STM tip positioned above an isolated Er atom (set point: $V_{dc} = 50$ mV, $I_{dc} = 50$ pA, $V_{rf} = 20$ mV, $B = 0.28$ T, $\theta = 97^\circ$).

4- Effect of the Er-Ti coupling on the ESR spectra of Ti

To qualitatively explain the effect of the coupling between Er and Ti on the ESR peaks of Ti, we consider both spins as two-level systems. Following Eq. 2 in the main text, we can define the dipolar interaction tensor $\bar{\bar{J}}_{\text{dip}}$ and the total interaction tensor $\bar{\bar{J}}_{\text{int}}$ as:

$$\mathbf{J}_{\text{Er}} \cdot \bar{\bar{J}}_{\text{dip}} \cdot \mathbf{S}_{\text{Ti}} \equiv H_{\text{dip}} \quad (\text{S1})$$

$$\bar{\bar{J}}_{\text{int}} = \bar{\bar{J}}_{\text{dip}} + J_{\text{exc}} \cdot \bar{\bar{1}}, \quad (\text{S2})$$

where J_{exc} is the exchange interaction energy expressed in terms of \mathbf{J}_{Er} (Eq. 2 in the main text) and $\bar{\bar{1}}$ is the identity tensor. For a fixed Er-Ti separation at a constant magnetic field angle, the total interaction tensor can be expressed as a scalar J_{int} . When the magnitude of J_{int} is smaller than the Zeeman energy of the two atoms, the ground state of the systems is the $|\downarrow\downarrow\rangle$ state, where the first and second arrow indicate the Ti and Er spin states, respectively (Fig. S4). At a finite magnetic field and when the interaction is close to zero (Fig. S4a,d), the two resonance frequencies of Ti coincide and only one peak is detected. This case corresponds to the pink spectrum in Fig. 1c in the main text and the spectrum in Fig. S3a. When a detectable interaction is present, the relative energy levels of $|\uparrow\downarrow\rangle$ and $|\downarrow\uparrow\rangle$ states shift with respect to the other two states and two peaks become distinguishable in the ESR spectrum. Depending on the sign of J_{int} , the interaction can be regarded as ferromagnetic (FM) if $J_{\text{int}} < 0$ (Fig. S4b,e) or antiferromagnetic (AFM) if $J_{\text{int}} > 0$ (Fig. S4c,f). The transition involving the ground state $|\downarrow\downarrow\rangle$ (f_1^{Ti}) is characterized by a higher ESR intensity due to its higher population. For this reason, a ferromagnetic interaction, which shifts the antiparallel levels $|\uparrow\downarrow\rangle$ and $|\downarrow\uparrow\rangle$ to higher energies, shows the higher intensity peak at higher frequencies. This type of interaction corresponds to the purple spectrum in Fig. 1c in the main text. The opposite is true for an antiferromagnetic interaction which shows the higher intensity peak at lower frequencies. The cases of AFM coupling can be seen in the spectra of the dimer with 0.72 nm separation (Fig. 2b, Fig. 4a in the main text and Fig. S11).

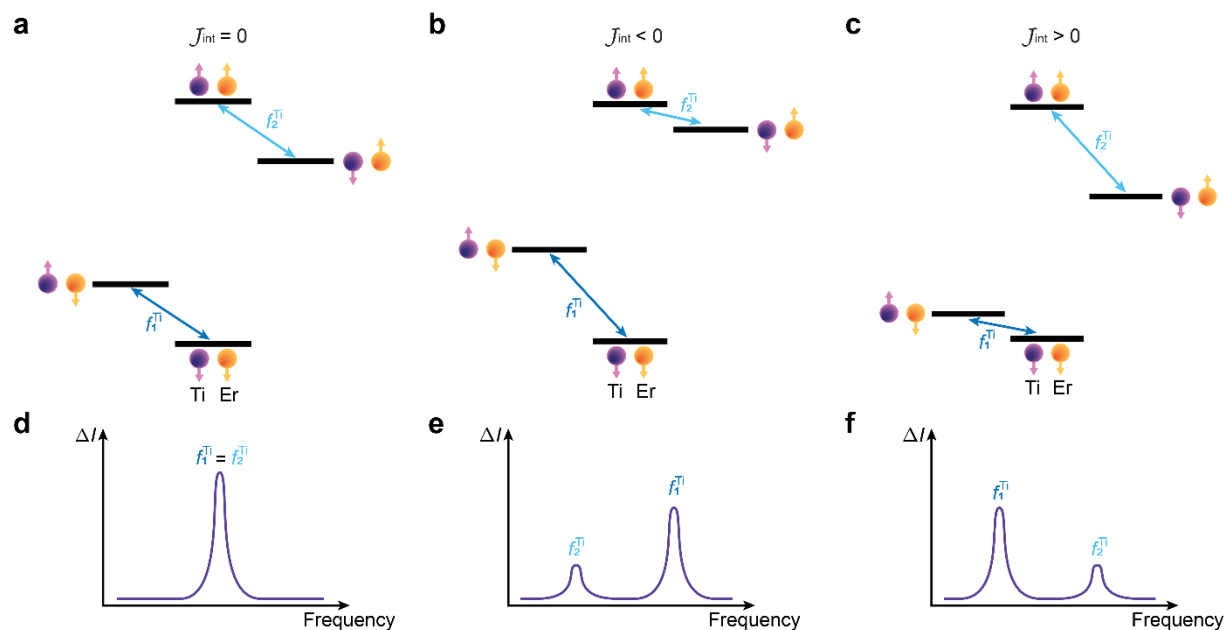


Figure S4 | Influence of the Er-Ti interaction on the energy levels and ESR spectra. **a,b,c**, Four-level scheme of Er-Ti dimers with $J_{\text{int}} = 0$, $J_{\text{int}} < 0$ (ferromagnetic) and $J_{\text{int}} > 0$ (antiferromagnetic) respectively. **d,e,f**, Schematics of the resulting ESR spectra on Ti in its resonance frequency range. When no interaction is present (**a**) only one peak is detectable (**d**). A ferromagnetic interaction ($J_{\text{int}} < 0$) shifts the antiparallel levels to higher energies (**b**), resulting in two distinguishable peaks with the higher intensity one (f_1^{Ti}) at a higher frequency (**e**). An antiferromagnetic interaction ($J_{\text{int}} > 0$) shifts the antiparallel levels to lower energies (**c**), resulting in two peaks with the higher intensity one (f_1^{Ti}) at a lower frequency (**f**).

5- Dimer with ^{167}Er

When measuring different Er-Ti dimers at the same separations (0.72 nm), we observed that a small fraction of them do not show any peak in the Er ESR transition range (Fig. S5). We ascribe this observation to the presence of ^{167}Er isotopes on the surface, which is the only observationally stable isotope of Er with a non-zero nuclear spin, present with a 22.9% abundance. This isotope presents a nuclear spin of $7\hbar/2$. When driving ESR transitions on this atom, a single ESR peak is expected to split into 8 peaks due to its hyperfine interaction with the nuclear spin². However, as for this atom the intensity of the Er ESR transition is also reduced by a factor of 8 and, thus, the ESR signal becomes too small to be detected in the present detection scheme. Nevertheless, this observation further supports the interpretation that f_3^{Er} and f_4^{Er} correspond to ESR transitions in the Er 4f spins since these transitions are the only ones that should be affected by the hyperfine interaction between the Er electron and nuclear spins.

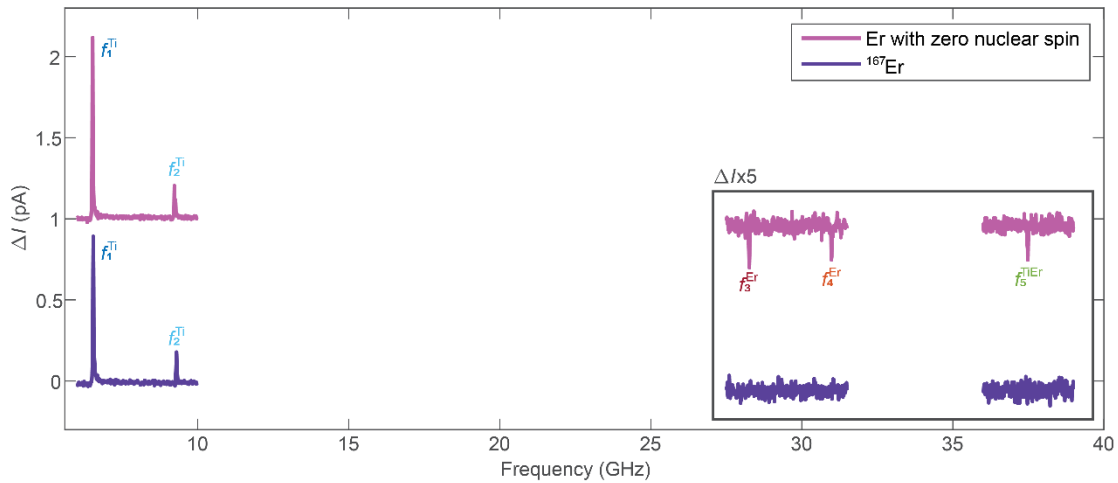


Figure S5 | Electron spin resonance on dimer containing ^{167}Er . ESR spectra acquired with the same STM tip on top of Ti in two different dimers: in the standard Er-Ti dimer (pink line, shifted in ΔI by 1 pA for readability) 5 peaks are detectable (f_1^{Ti} , f_2^{Ti} , f_3^{Er} , f_4^{Er} and f_5^{TiEr}) while in the dimer containing ^{167}Er with nuclear spin $7\hbar/2$ (purple line), only f_1^{Ti} and f_2^{Ti} (related to Ti transitions) are detectable (set point: $V_{\text{dc}} = 60$ mV, $I_{\text{dc}} = 20$ pA, $V_{\text{rf}} = 15$ mV, $B = 0.3$ T, $\theta = 52^\circ$).

6- Electron spin resonance spectra with out-of-plane magnetic fields

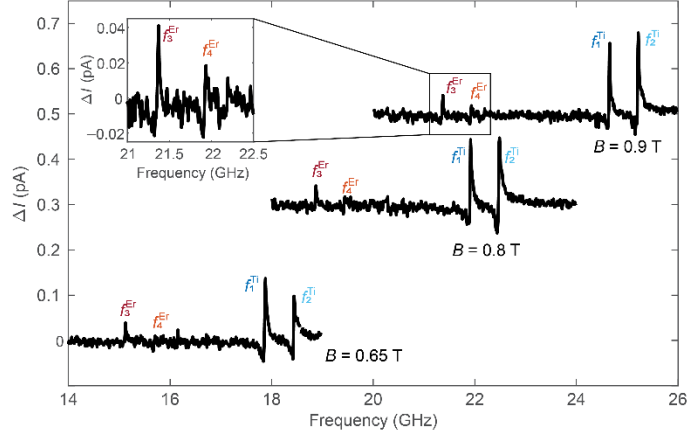


Figure S6 | Electron spin resonance at out-of-plane magnetic fields. ESR spectra measured on the Er-Ti dimer with 0.72 nm separation at different magnetic fields close to the out-of-plane direction ($\theta = 7^\circ$): $B = 0.65$ T, 0.8 T, and 0.9 T (set point: $V_{dc} = 70$ mV, $I_{dc} = 20$ pA, $V_{rf} = 25$ mV). The spectra at $B = 0.8$ T and 0.9 T were shifted in ΔI by 0.3 pA and 0.5 pA, respectively, for clarity. The inset on the top left corner shows a zoomed-in spectrum of the peaks f_3^{Er} and f_4^{Er} .

When we applied the magnetic field close to the out-of-plane direction ($\theta = 7^\circ$), we observed 4 ESR peaks (Fig. S6). As explained in the main text, when the magnetic field is applied along the out-of-plane direction ($\theta = 0^\circ$), the expectation value of \mathbf{J}_{Er} is $\hbar/2$ similarly to \mathbf{S}_{Ti} . However, the Er g-factor is 1.2, while Ti has a g-factor of 1.989 ± 0.024^3 . The peaks at lower frequencies, thus, correspond to the Er ESR transitions (f_3^{Er} and f_4^{Er}) due to the smaller Zeeman energy of Er than the one of Ti. To further clarify the identification of ESR peaks, we measured the ESR spectra at different magnitudes of magnetic fields at $\theta = 7^\circ$ and followed the linear dependence of their resonance frequencies on the magnetic field magnitudes.

7- Electron spin resonance spectra close to the level crossing

When the magnetic field is applied at about 12° from the normal to the surface ($\theta \sim 12^\circ$), we expect Er and Ti to have similar Zeeman splittings. In this situation, the intermediate energy levels of the Er-Ti dimer with 0.72 nm separation must be regarded as singlet ($\frac{1}{\sqrt{2}}|\uparrow\downarrow\rangle - \frac{1}{\sqrt{2}}|\downarrow\uparrow\rangle$) and triplet states⁴ ($\frac{1}{\sqrt{2}}|\uparrow\downarrow\rangle + \frac{1}{\sqrt{2}}|\downarrow\uparrow\rangle$) as explained in the main text. In Fig. S7, we show three ESR spectra acquired around the expected matching angle, i.e. $\theta = 14.5^\circ$, 17° , and 22° . At $\theta = 22^\circ$, all four ESR transitions from f_1^{Ti} to f_4^{Er} are visible, with f_3^{Er} and f_4^{Er} observed at higher frequencies than f_1^{Ti} and f_2^{Ti} . In addition, the different peak intensities between f_1^{Ti} and f_2^{Ti} (with the intensity of f_1^{Ti} larger than f_2^{Ti}) indicate an antiferromagnetic coupling between Er and Ti⁵. Conversely, for both $\theta = 17^\circ$ and $\theta = 14.5^\circ$, it is not possible to identify the f_3^{Er} and f_4^{Er} peaks stemming from Er ESR transitions. Nevertheless, for both spectra measured for $\theta \leq 17^\circ$ the asymmetric intensity of f_1^{Ti} and f_2^{Ti} is reversed, suggesting a change of the system configuration possibly due to the close match between the Er and Ti levels at around $\theta = 12^\circ$. As discussed in the main text, close to $\theta = 12^\circ$ the energy levels of the system cannot be represented as Zeeman product states and for this reason the detection mechanism for both Ti and Er peaks explained in the main text may not be valid in this range of θ .

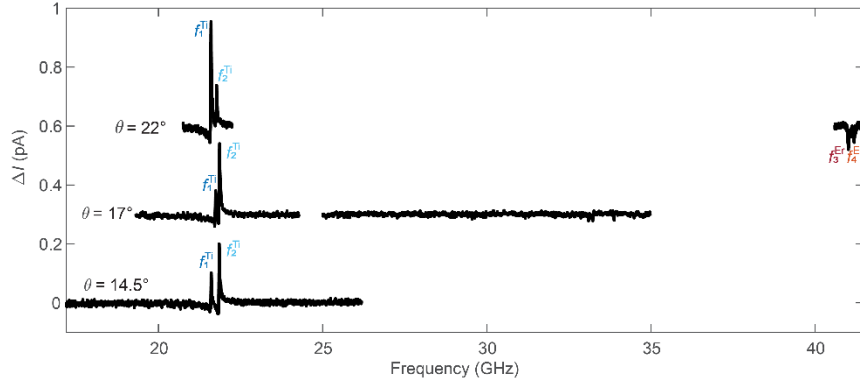


Figure S7 | Electron spin resonance close to the level crossing point. ESR spectra on the Ti atom of the 0.72 nm dimer at $\theta = 14.5^\circ$, 17° and 22° (set point: $V_{dc} = 70$ mV, $I_{dc} = 12$ pA, $V_{rf} = 20$ mV, $B = 0.8$ T). The spectra at $\theta = 17^\circ$ and $\theta = 22^\circ$ were shifted in ΔI by 0.3 pA and 0.6 pA, respectively, for clarity.

8- Tip position dependence of ESR signals on the Er-Ti dimer

As mentioned in the main text, when the tip is positioned above the Ti atom in the Er-Ti dimer with 0.72 nm separation, we can resolve up to 5 ESR peaks. However when we move the tip away from the Ti center, the peaks related to the Er ESR transitions decrease in intensity (Fig. S8). When the tip is about 0.3 nm from the Ti center the intensity of the peaks is too low to be resolved (spectrum 2). In a similar way, when the tip is positioned above Er no peaks are detectable (spectrum 1).

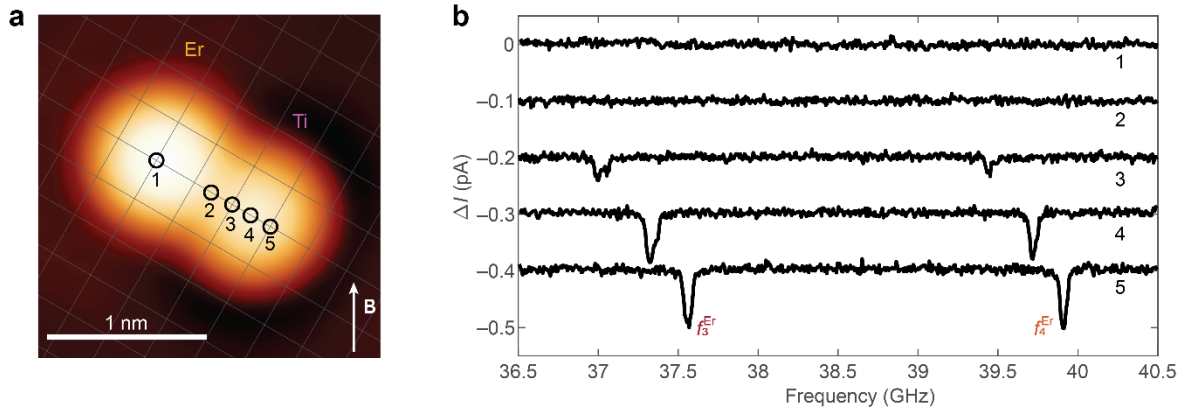


Figure S8 | Electron spin resonance at different tip locations on the Er-Ti dimer. **a**, STM image of the Er-Ti dimer with 0.72 nm separation (set-point: $V_{dc} = 100$ mV, $I_{dc} = 20$ pA) superimposed with a grid representing the oxygen site of MgO lattice. The different locations where the tip was positioned during the ESR measurement are depicted as black circles numbered from 1 to 5. **b**, Corresponding ESR spectra at different tip locations as marked in (a) (set-point: $V_{dc} = 70$ mV, $I_{dc} = 12$ pA, $V_{rf} = 25$ mV, $B = 0.28$ T, $\theta = 97^\circ$). When the tip is approached laterally to the Er atom, the Er ESR peaks, f_3^{Er} and f_4^{Er} , shift to lower frequencies due to the antiferromagnetic interaction between the Er atom and the magnetic tip. The intensity of the peaks decreases with moving the tip away from the Ti atom and no peaks are detectable at a distance of 0.3 nm from its center (spectrum 2). The spectra 2, 3, 4 and 5 were shifted vertically by -0.1 pA, -0.2 pA, -0.3 pA and -0.4 pA, respectively, for clarity.

9- Rate equation model

To reproduce the different sign of the peaks of the Er ESR transitions shown in Fig. 3a, as well as the dependence of the peak intensity as a function of the driving strength (V_{rf}) displayed in Fig. 3b of the main text, we developed a rate equation model based on 4 differential equations:

$$\begin{aligned} \frac{dn_{00}}{dt} &= -(W_1 + \Gamma_{1-}^{\text{Ti}})n_{00} - (W_3 + \Gamma_{3-}^{\text{Er}})n_{00} + (W_1 + \Gamma_{1+}^{\text{Ti}})n_{10} + (W_3 + \Gamma_{3+}^{\text{Er}})n_{01} \\ \frac{dn_{10}}{dt} &= -(W_1 + \Gamma_{1+}^{\text{Ti}})n_{10} - (W_4 + \Gamma_{4-}^{\text{Er}})n_{10} + (W_1 + \Gamma_{1-}^{\text{Ti}})n_{00} + (W_4 + \Gamma_{4+}^{\text{Er}})n_{11} \\ \frac{dn_{01}}{dt} &= -(W_2 + \Gamma_{2-}^{\text{Ti}})n_{01} - (W_3 + \Gamma_{3+}^{\text{Er}})n_{01} + (W_2 + \Gamma_{2+}^{\text{Ti}})n_{11} + (W_3 + \Gamma_{3-}^{\text{Er}})n_{00} \\ \frac{dn_{11}}{dt} &= -(W_2 + \Gamma_{2+}^{\text{Ti}})n_{11} - (W_4 + \Gamma_{4+}^{\text{Er}})n_{11} + (W_2 + \Gamma_{2-}^{\text{Ti}})n_{01} + (W_4 + \Gamma_{4-}^{\text{Er}})n_{10} \end{aligned} \quad (\text{S3})$$

Here, n_x is the population of the level x , W_y is the driving of the transition y , and Γ_y is the relaxation rate of the levels connected by the transition y . The “+” and “-” subscripts in the relaxation rates indicate if the relaxation is towards a lower energy level (+) or a higher energy level (-), such that the total relaxation can be written as $\Gamma_y = \Gamma_{y+} + \Gamma_{y-}$. We distinguish the total relaxation rates for Er and Ti by computing $\Gamma^{\text{Er}} = 1/T_1^{\text{Er}}$ and $\Gamma^{\text{Ti}} = 1/T_1^{\text{Ti}}$. In addition, we conserve the total population, $n_{00} + n_{10} + n_{01} + n_{11} = 1$. To obtain the steady state solution we set the derivatives equal to zero. By considering a specific driving W_y and solving the set of equations in the steady state, we obtain the population of each level. In Fig. S9a, a schematic of the four-level system is reported with the respective population at thermal equilibrium for each level (the rough numbers for the populations were calculated considering a temperature of 1.3 K and using the energy differences between levels obtained from the ESR peaks of Fig. 2b at $B = 0.3$ T and $\theta = 97^\circ$). By driving f_3^{Er} into saturation, we can equalize the populations of the $|\downarrow\downarrow\rangle$ and $|\downarrow\uparrow\rangle$ states, which makes the system far from the thermal equilibrium state (Fig. S9b). Given that the spin relaxation of Er is much slower than one for Ti, the system tends to relax through a Ti relaxation event (dotted purple arrows in Fig. S9b). The relaxation from $|\downarrow\uparrow\rangle$ to $|\uparrow\uparrow\rangle$ will be dominated by upward events while from $|\uparrow\downarrow\rangle$ to $|\downarrow\downarrow\rangle$ by downward ones. Finally, by including all the relaxation paths in the model, the population of each level evolves to the steady state reported in Fig. S9c.

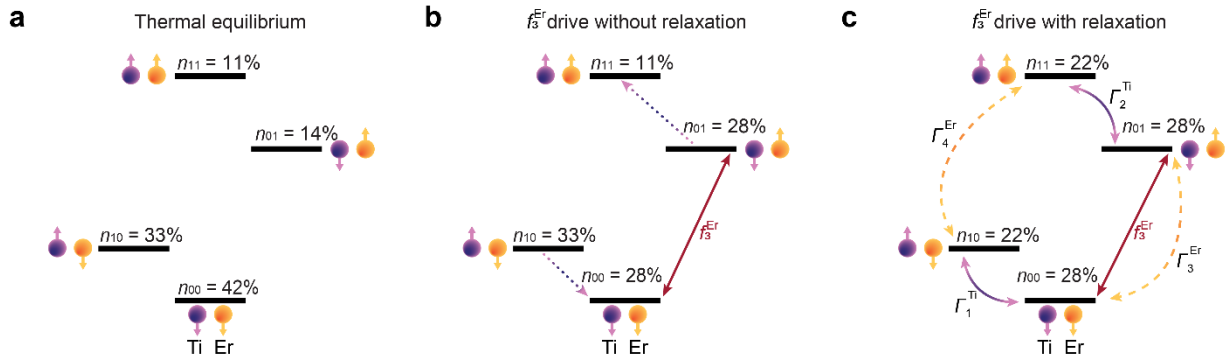


Figure S9 | Populations of the Er-Ti dimer calculated with the rate equation model at different conditions. **a**, Four-level scheme and respective populations for each level at thermal equilibrium. **b**, Driving the system into resonance at f_3^{Er} (shown as solid red arrow) and prior to activating the relaxation terms described in the model. The ESR driving leads to an equalization of n_{00} and n_{01} , which makes the Ti populations far from the Boltzmann distribution. Dashed arrows represent the relaxation path realized by the Ti relaxation mechanism, where part of the population of n_{10} is transferred to n_{00} through downward relaxation mechanism. The rf excitation re-equilibrates the excess of population towards n_{01} , which is further transferred to n_{11} via upward

Ti relaxation mechanisms. c, Resulting populations after the inclusion of the relaxation terms, with the Er relaxation shown as dashed yellow arrows and the Ti relaxation as pink solid arrows.

In the rate equation model, we included the spin pumping term (ζ) as a shift of the population of the levels given by the angular momentum transfer from the tunneling electrons into Ti, as follows:

$$\begin{aligned}
 n_{00}^{\text{spin pumping}} &= n_{00} - \zeta \\
 n_{10}^{\text{spin pumping}} &= n_{10} + \zeta \\
 n_{01}^{\text{spin pumping}} &= n_{01} - \zeta \\
 n_{11}^{\text{spin pumping}} &= n_{11} + \zeta
 \end{aligned} \tag{S4}$$

We used the rate equation model to fit the V_{rf} dependence of the peak intensity in Fig. 3b. We set $T_1^{\text{Ti}} = 10 \text{ ns}^6$ and $T_1^{\text{Er}} = 818 \text{ ns}$. We used two different driving terms for Er and Ti transitions: $W^{\text{Ti}} = W_1 = W_2 = A^{\text{Ti}} V_{\text{rf}}^2$ and $W^{\text{Er}} = W_3 = W_4 = A^{\text{Er}} V_{\text{rf}}^2$, where $A^{\text{Ti,Er}}$ is the respective scaling factor for the ESR driving of Ti and Er. The fitting parameters are A^{Ti} , A^{Er} and the spin pumping term ζ . The fitting yielded $A^{\text{Ti}} = 14917$, $A^{\text{Er}} = 29338$ and a negative spin pumping of -0.94% . The driving term can be expressed as $W = T_2 \Omega^2 / 2^7$. The rabi rate Ω depends on the strength of the modulation provided by the tip-atom or atom-atom coupling and it is linear with V_{rf} and, thus, the scaling factor A . A four-level scheme depicting all the terms present in the rate equation model is given in Fig. S10a. As discussed in the main text and in the previous section, the Er-Ti coupling is 3–4 times smaller than Fe-Ti dimers used for remote ESR of $3d$ electrons^{8,9}. Therefore, we expect a lower Rabi rate for Er since its driving comes from the modulation of its magnetic interaction with Ti. On the other hand, the fit yields a driving factor A^{Er} larger than A^{Ti} , which suggests a much longer T_2 of Er compared to other $3d$ elements, possibly due to the well protected $4f$ orbitals. The spin pumping term ζ is required to account for the different sign of the Er peaks observed with different ESR tips, as shown in Fig. 3a in the main text. As discussed in the following, our model indicates that a negative ζ produces negative Er peaks while the opposite is true for a positive ζ . The Ti ESR peaks are minimally influenced by ζ . In Fig. S10b, we show the effect of ζ on f_3^{Er} in the rate equation model. In the absence of spin pumping, a small positive signal is predicted. This is due to the difference in energy between the ESR transitions f_1^{Ti} and f_2^{Ti} which leads to an intrinsic difference between Γ_1^{Ti} and Γ_2^{Ti} . Finally, the intensity of the ESR signal is calculated as the difference between the populations of the Ti \uparrow states ($n_{10} + n_{11}$) and Ti \downarrow states ($n_{00} + n_{01}$) compared to the undriven state:

$$\Delta I = C \cdot \{[(n_{10} + n_{11}) - (n_{00} + n_{01})]_{\text{rf1}} - [(n_{10} + n_{11}) - (n_{00} + n_{01})]_{\text{undriven}}\}, \tag{S5}$$

where C is a scaling factor which considers the polarization of the tip and the contribution of the magnetic shell on the spin polarized current. To reproduce the experimental results, we use $C = 45.2 \text{ pA}$. The driven populations are calculated using the differential equations of Eq. S3 and the undriven populations using the ones obtained from Eq. S4.

To reproduce the ESR intensity ratios as a function of V_{rf2} in Fig. 4c, a similar model was employed. With the only difference being the calculation of the ESR intensity as:

$$\Delta I_{\text{double resonance}} = C \cdot \{[(n_{10} + n_{11}) - (n_{00} + n_{01})]_{\text{rf1,rf2}} - [(n_{10} + n_{11}) - (n_{00} + n_{01})]_{\text{rf2}}\} \tag{S6}$$

where the driven populations are obtained through Eq. S1 with the application of a simultaneous driving from rf1 and rf2 and subtracted to the population obtained with a single drive rf1 to reproduce the double resonance experiment⁹.

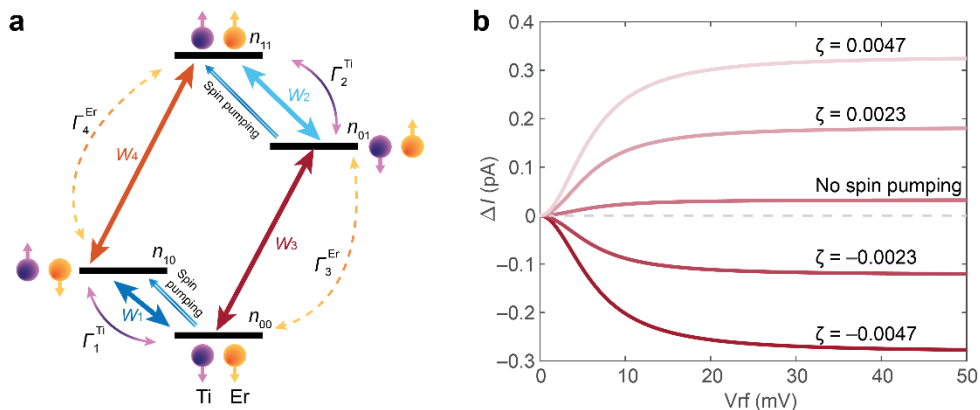


Figure S10 | Rate equation model and spin pumping dependence of the Er ESR signal. **a**, 4-level scheme relative to the rate equation model describing the driving term (W), relaxation rates (Γ) and a positive spin pumping term (ζ). **b**, Effect of the spin pumping term for the f_3^{Er} peak intensity (ΔI) as a function of V_{rf} predicted by the rate equation model. A negative ζ produces a negative ESR signal while a positive ζ produces a positive ESR signal. When the spin pumping is excluded from the model, a slightly positive ESR signal is predicted.

10- Measurement of Rabi oscillations

To measure Rabi oscillations on Ti and Er atoms in a Er-Ti dimer, we followed a procedure similar to the one used in ⁶. With the STM tip positioned on top of the Ti atom in the Er-Ti dimer with 0.72 nm separation, we applied a series of V_{rf} pulses at the resonance frequency of f_1^{Ti} (Fig. a) and f_3^{Er} (Fig. S11b) with increasing pulse widths. We subtracted a linear fit to the data in order to remove the rf rectified current given by the nonlinearity of the I - V curve¹⁰. When we apply rf pulses at the resonance frequency of f_1 we can resolve Rabi oscillations in the Ti spin (Fig. S11a). The fit of the signal measured on a Ti atom with an exponentially decaying sinusoidal function yields a Rabi rate Ω_{Ti} of 435 ± 41 MHz and a $T_{2\text{Rabi}}^{Ti}$ of 9.9 ± 3.4 ns. On the other hand, when we apply rf pulses at the resonance frequency of f_3 , no Rabi oscillation is observed. The monotonic decrease of the signal is due to the negative sign of the f_3 peak, which reaches saturation for sufficiently long rf pulses.

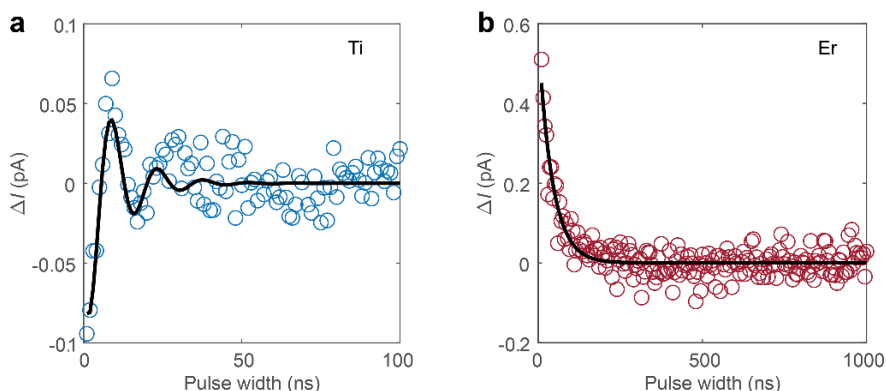


Figure S11 | Rabi measurements. **a**, Pulsed ESR measured with the STM tip on the Ti atom of the Er-Ti dimer with 0.72 nm separation. With the pulses applied at the resonance frequency of f_1^{Ti} , Rabi oscillations for the Ti spin are clearly observed (set-point: $V_{dc} = 20$ mV, $I_{dc} = 10$ pA, $V_{rf} = 70$ mV, $B = 0.288$ T, $\theta = 97^\circ$). The black line is a fit using an exponentially decaying sine function. **b**, Pulsed ESR measured with the STM tip on the Ti atom of the same dimer but with the pulses at the resonance frequency of f_3^{Er} (set-point: $V_{dc} = 70$ mV, $I_{dc} = 50$ pA, $V_{rf} = 90$ mV, $B = 0.288$ T, $\theta = 97^\circ$). The black line is an exponential fit as a guide for the eye.

References

- 1 Loth, S. *et al.* Controlling the state of quantum spins with electric currents. *Nature Physics* **6**, 340-344 (2010). <https://doi.org:10.1038/nphys1616>
- 2 Willke, P. *et al.* Hyperfine interaction of individual atoms on a surface. *Science* **362**, 336-339 (2018). <https://doi.org:doi:10.1126/science.aat7047>
- 3 Kim, J. *et al.* Spin resonance amplitude and frequency of a single atom on a surface in a vector magnetic field. *Physical Review B* **104**, 174408 (2021). <https://doi.org:10.1103/PhysRevB.104.174408>
- 4 Bae, Y. *et al.* Enhanced quantum coherence in exchange coupled spins via singlet-triplet transitions. *Science Advances* **4**, eaau4159 (2018). <https://doi.org:doi:10.1126/sciadv.aau4159>
- 5 Yang, K. *et al.* Engineering the Eigenstates of Coupled Spin-1/2 Atoms on a Surface. *Physical Review Letters* **119**, 227206 (2017). <https://doi.org:10.1103/PhysRevLett.119.227206>
- 6 Yang, K. *et al.* Coherent spin manipulation of individual atoms on a surface. *Science* **366**, 509-+ (2019). <https://doi.org:10.1126/science.aay6779>
- 7 Reiter, F. & Sørensen, A. S. Effective operator formalism for open quantum systems. *Phys. Rev. A* **85**, 032111 (2012). <https://doi.org:10.1103/PhysRevA.85.032111>
- 8 Phark, S.-h. *et al.* Electric-Field-Driven Spin Resonance by On-Surface Exchange Coupling to a Single-Atom Magnet. *Advanced Science* **n/a**, 2302033 (2023). <https://doi.org:https://doi.org/10.1002/advs.202302033>
- 9 Phark, S.-h. *et al.* Double-Resonance Spectroscopy of Coupled Electron Spins on a Surface. *ACS Nano* **17**, 14144-14151 (2023). <https://doi.org:10.1021/acsnano.3c04754>
- 10 Paul, W., Baumann, S., Lutz, C. P. & Heinrich, A. J. Generation of constant-amplitude radio-frequency sweeps at a tunnel junction for spin resonance STM. *Rev. Sci. Instrum.* **87** (2016). <https://doi.org:10.1063/1.4955446>